Characterizing Near-Field Surface Deformation in the 1990 Rudbar Earthquake (Iran) Using Optical Image Correlation

Najmeh Ajorlou, James Hollingsworth, Zahra Mousavi, Abdolreza Ghods, Zohreh Masoumi

HAL Id: hal-03454844
https://hal.science/hal-03454844

Submitted on 17 Mar 2022

Key Points:

- We characterize the surface displacement field associated with the 1990 Rudbar earthquake using new optical image correlation techniques
- We find the average surface slip ~2.2 m, with a maximum displacement of ~6.5 m along Zard Geli eastern part of the fault rupture
- We find that off-fault deformation is unusually high, and appears to vary as a function of the fault geometric roughness

Characterizing Near-Field Surface Deformation in the 1990 Rudbar Earthquake (Iran) Using Optical Image Correlation

Najmeh Ajorlou[1] , **James Hollingsworth[2]** , **Zahra Mousavi[1]** , **Abdolreza Ghods[1]**, and **Zohreh Masoumi[1]**

[1]Department of Earth Science, Institute for Advanced Studies in Basic Sciences, Zanjan, Iran, [2]Université Grenoble Alpes, Université Savoie Mont Blanc, CNRS, IRD, Université Gustave Eiffel, Grenoble, France

Abstract The 1990 Rudbar earthquake (Mw 7.3) broke along three right-stepping segments of the left-lateral Rudbar fault, in the western Alborz mountains (Iran), producing ~80 km of surface rupture. Previously reported horizontal (~60 cm) field offsets were surprisingly low, and the vertical (~95 cm) unexpected, given the relatively large moment release, shallow source depth, vertical fault geometry, and left-lateral rake. We characterize the surface displacement from optical image correlation of satellite and aerial images. A maximum displacement of ~6.5 m is observed in the eastern part of the rupture consistent with both a sharp pulse in the moment release rate ~10 s after the rupture initiation, and the macroseismic isoseismal curves. We find ~2.2 m mean surface slip, larger than field measurements, but consistent with empirical scaling laws based upon the seismological moment release. Estimates of fault zone width based on correlation of 1 m resolution aerial photos (and corrected for smoothing bias) are <200 m; these values increase artificially with lower resolution imagery, which is more affected by smoothing bias. The large mismatch between field and correlation displacements suggests the Rudbar earthquake probably featured significant off-fault deformation, consistent with its low structural maturity. Finally, we document a surface rupture along a structural continuation of the Kabateh segment, east of the Sefid Rud river. Slip along this segment (1–2 m), is less than the neighboring Zard Geli segment (1.5–6 m). The two faults converge at Sefid Rud, which appears to represent a major structural feature controlling fault segmentation in this region.

Plain Language Summary The 1990 (Mw 7.3) Rudbar earthquake was one of the most destructive earthquakes to have affected Iran in recent history. However, despite the relatively large size of the earthquake, field surveys revealed surprisingly small (<1 m) left-lateral offsets. We resolve this long-standing problem using new optical correlation techniques, which allow us to fully document the earthquake surface displacement. Left-lateral offsets reached up to 5-6 m along the Zard Geli fault segment, while new surface ruptures are reported along a failed branch of the rupture east of the Sefid Rud river valley. Our results indicate that slip was relatively continuous between various fault segments, with slip becoming distributed in the fault linkage zones. We find that OFD is unusually high, and appears to vary as a function of the fault geometric roughness. This study highlights the power of optical image correlation for revisiting past earthquakes and providing valuable new constraints on surface ruptures in general. With this approach, we may thus expand the catalog of earthquakes that have robust measurements of on- vs off-fault slip, which will be essential for characterizing the parameters that control the localization of coseismic slip, and how we engineer for future surface rupturing earthquakes.

1. Introduction

On June 20, 1990, the devastating Mw 7.3 Rudbar earthquake struck the NW Alborz region of Iran, killing ~15,000 people, and leaving ~500,000 people homeless, and destroying three cities and 700 villages in the region (Berberian et al., 1992; Berberian & Walker, 2010). The earthquake occurred on a previously unknown left-lateral strike-slip fault in the western Alborz mountains (Figure 1), and produced a surface rupture ~80 km long on a near-vertical fault plane (Berberian et al., 1992). Point-source inversions of *P* and SH waves indicated predominantly left-lateral slip (e.g., Berberian et al., 1992; Campos et al., 1994) on a ESE-WNW (~300°) striking fault. Somewhat at odds with the non-oblique earthquake source model, sparse
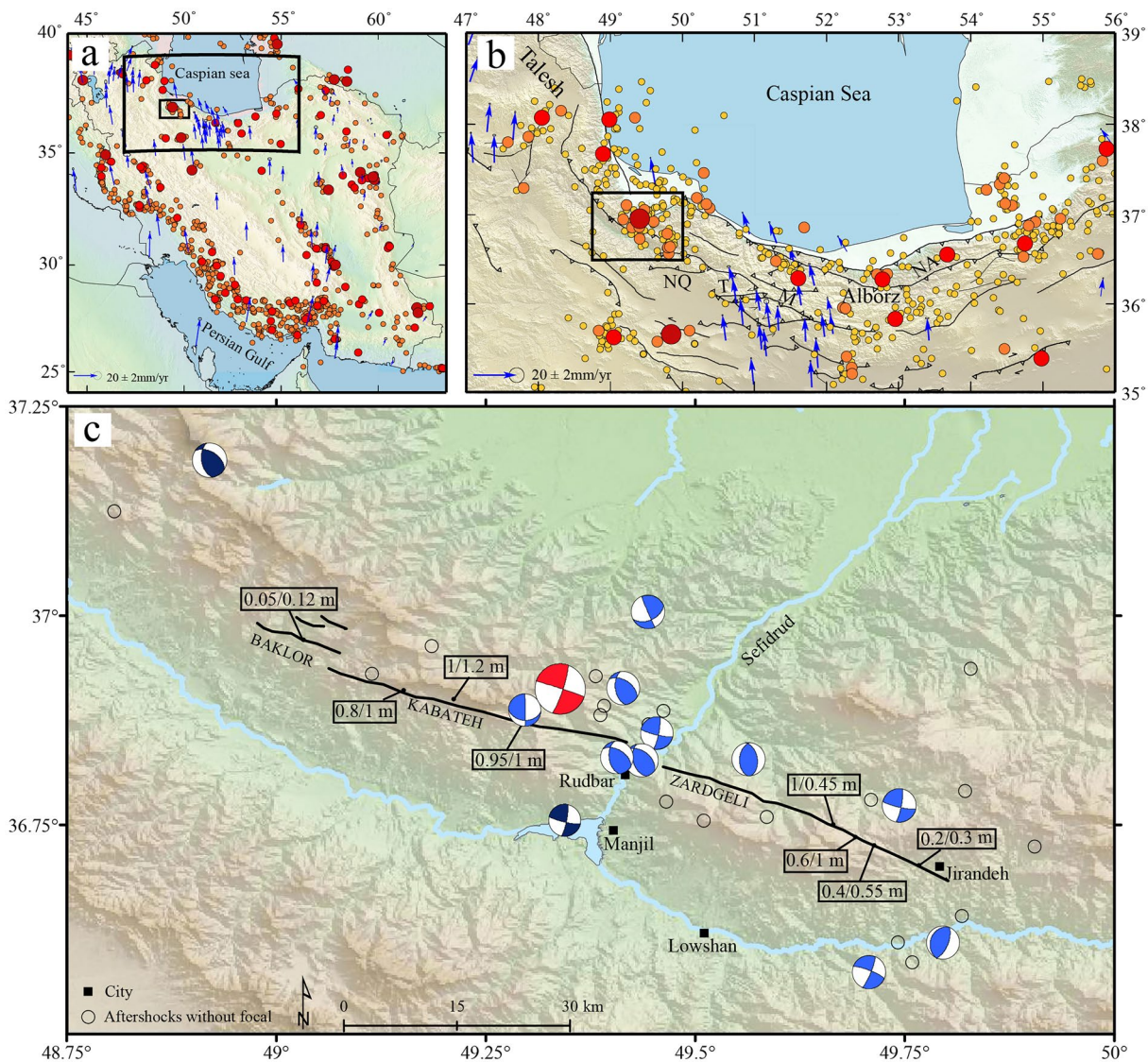
Figure 1. Study area. (a) The seismotectonics map within Iranian political boarder, The large and small rectangles present the location of panel b and c, respectively. The seismicity with magnitude larger than five from USGS earthquake catalog (https://earthquake.usgs.gov/earthquakes/search/) are presented by orange (Mw > 5), red (Mw > 6), and dark red (Mw > 7) circles. Blue vectors show GPS velocities throughout Iran (Khorrami et al., 2019). (b) The active tectonics of the Alborz mountain belt. Yellow (>4), orange (>5), red (>6), and dark red (>7) circles indicate seismicity in the Alborz mountain belt. Letters indicate various faults: NQ (North Qazvin), T (Taleqan), M (Mosha), NA (North Alborz) reported by Hessami et al. (2003). (c) The black solid lines present the Rudbar fault trace mapped by Berberian and Walker (2010). The numbers in the black boxes are horizontal/vertical displacements reported by Berberian and Walker (2010). The red and blue (light and dark) beach balls represent the focal mechanisms of the mainshock and aftershocks, respectively (Gao & Wallace, 1995; Jackson et al., 2002). The calibrated earthquake Locations of the mainshock and various aftershocks are from https://www.sciencebase.gov/catalog/item/5de542cae4b02caea0e8fa90 (in light blue beach balls and unfilled black circles) and EHB catalog in dark blue (International Seismological Center, EHB Bulletin, http://www.isc.ac.uk, International Seismological Centre, United Kingdom, 2009).

field measurements revealed average left-lateral displacements of ∼60 cm with vertical displacements of ∼95 cm (Berberian et al., 1992; Berberian & Walker, 2010). Subsequent investigation of the aftershocks was limited to teleseismic analysis, and thus unable to reveal many details on the location of the mainshock rupture plane (Berberian et al., 1992; Gao & Wallace, 1995).

Simple estimates of the average fault displacement, assuming a seismic moment of ∼8.8e + 19 Nm (Gao & Wallace, 1995) and down-dip fault width of 15–20 km (Berberian et al., 1992; Tatar & Hatzfeld, 2009) indicate 1.8–2.4 m of left-lateral slip (which increases for a narrower depth range); significantly higher than the observed maximum horizontal surface displacements of 60 cm (Figure 1c) (Berberian & Walker, 2010),

and potentially implying a large decrease in slip as the rupture propagated toward the surface ("shallow slip deficit," see Fialko et al., 2005).

In this work we use optical geodesy techniques (correlation of optical satellite and aerial images spanning the earthquake) to document the location of the rupture, and characterize the style and magnitude of a long-strike surface displacement. The aim is to reconcile the range of observations for this earthquake, examine controls on magnitudes of surface offsets, and the impact of this earthquake on surrounding faults. Given the Rudbar earthquake occurred prior to the availability of modern geodetic techniques, such as GPS and InSAR, optical image correlation (OIC) is the only geodetic method available to retrospectively study the coseismic displacement field of the Rudbar earthquake. The OIC method is well-suited to studying strike-slip faults, especially in arid regions characterized by sparse surface vegetation and subdued topography (Avouac et al., 2006; Milliner et al, 2015, 2016; Zhou et al., 2016; Zinke et al., 2014). However, the rugged topography of the Rudbar region presents a processing challenge, as residual stereoscopic signal can easily overwhelm any tectonic signal unless care is taken in the image processing steps to isolate and remove it. Furthermore, dense vegetation, which degrades the correlation process, covers the central part of the rupture, east of the Sefid Rud River. Therefore, we develop a new robust processing workflow, which takes advantage of the open-source Ames-Stereo Pipeline software (Beyer et al., 2018), and existing 3D correlation approaches (Zinke et al., 2019) to precisely co-register, orthorectify and correlate all imagery. Detailed knowledge of the location and along-strike variability of the Rudbar surface rupture provides important new observational constraints needed to (1) reconcile seismic, geodetic, remote, and field-based observations of coseismic slip, (2) reassess seismic hazard for the region, including estimation of how co-seismic stress changes impact potential failure of neighboring fault systems, and (3) address which geological factors (e.g., lithologic, topographic, structural) may control the degree of surface slip variability and localization in large surface-rupturing earthquakes. The latter point is significant, as rough faults are more likely to produce the destructive strong ground motions that pose a major risk to populations affected by large surface-rupturing earthquakes.

2. Tectonic and Geological Background

2.1. Regional Tectonics and Geographic Setting

The Alborz mountains of North Iran were formed during the initial stages of the Arabia-Eurasia collision, during the Late Eocene-Early Oligocene (∼34 Ma—see Alavi, 1996; Berberian, 1983, Rezaeian et al., 2012). Since this time, the Alborz has experienced several phases of enhanced exhumation, during the Mid-Miocene and Plio-Quaternary (Rezaeian et al., 2012). At the present day, the Alborz mountains accommodate 25% of the northward motion of Arabia, with respect to Eurasia, in a transpressional orogen bounded to the north by the South Caspian block, and the south by the Central Iranian block (Allen et all., 2003; Djamour et al., 2010; Jackson et al., 2002; Khorrami et al., 2019; Vernant, Nilforoushan, Hatzfeld, et al., 2004). Oblique shortening is accommodated across the Alborz, in response to the continued northward motion of Arabia relative to Eurasia, and the westward motion of the South Caspian block, relative to Eurasia (Jackson et al., 2002). GPS velocities indicate 5 ± 2 mm/yr NS-shortening is accommodated across the Alborz, while 4 ± 2 mm/yr left-lateral shear is accommodated across various strike-slip faults, which are generally internal to the range (Figure 1a–1b), e.g. Mosha Fault, Taleqan Fault, Rudbar Fault, etc, (Khorrami et al., 2019; Vernant, Nilforoushan, Chery, et al., 2004; Vernant, Nilforoushan, Hatzfeld, et al., 2004).

The Alborz extend ∼600 km east-west across northern Iran, separating the wet lowlands of the South Caspian depression to the north from the arid highlands of the Iranian Plateau to the south. Mean elevations reach ∼3000 m (Central Alborz), with range-perpendicular widths of 50–150 km (the range narrows at lower elevations). The trend of the main folds and thrust structures varies from ENE (N80°E) in the East Alborz, east of 53°E, to WNW (N110°E) in the West Alborz, west of 53°E.

The 1990 Rudbar earthquake struck the West Alborz region, close to where the Sefid Rud River transects the range, draining waters northeast from Central Iran into the South Caspian Sea (Figure 1c). The Sefid Rud follows a structural lineament known as the Lahijan Fault Zone (Berberian, 1983; Rezaeian et al., 2020; Figure 2), which separates the Western Alborz from the Talesh range. Stratigraphically and structurally, the Talesh represent a western continuation of the Alborz range (Madanipour et al., 2017), wrapping around the
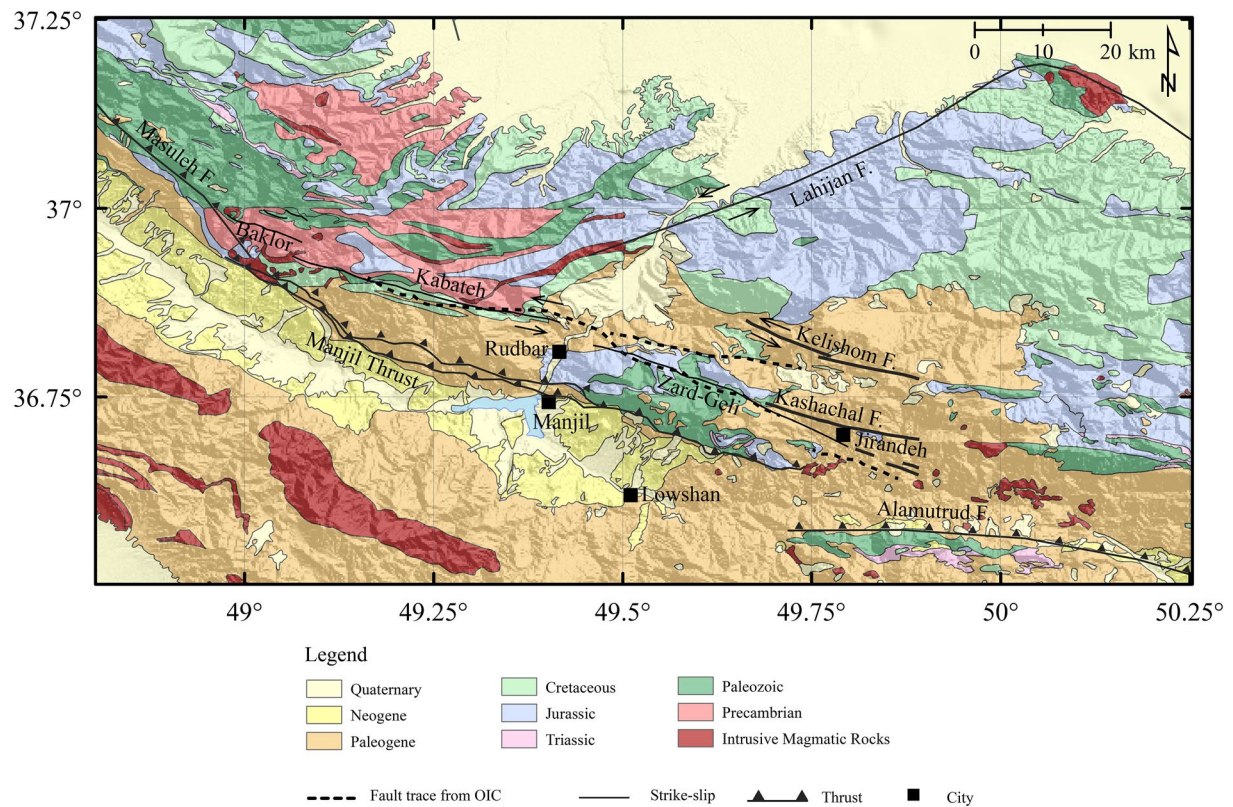
Figure 2. Geological map of the study area (compiled and modified from Geological Survey of Iran 1:250,000 geological map). The black dash line presents the fault trace we mapped from cross correlation of SPOT images, other faults reported by Berberian and Walker (2010) and Hessami et al. (2003). The small black squares show location of cities.

SW corner of the South Caspian in response to the ongoing Arabia-Eurasia collision (Jackson et al., 2002), before finally terminating in Azerbaijan.

Based on rigid block modeling of the horizontal GPS velocity field (Djamour et al., 2010; Khorrami et al., 2019), at the longitude of ~49.5°E, shortening across the Alborz is thought to be accommodated primarily on the north-dipping Manjil thrust, and the south-dipping Khazar thrust faults, which bound the range to the south and north, respectively. Left-lateral shear, induced by the western motion of the rigid South Caspian block, relative to Eurasia, is accommodated on the Rudbar, Kelishom, and Kashachal Faults, which are internal to the range (Berberian & Walker, 2010; Figure 2).

The geology of the West Alborz is characterized by Late Precambrian to Eocene sedimentary units, and Late Precambrian to Quaternary volcanic rocks (Figure 2; Stöcklin, 1974; Tatar & Hatzfeld, 2009). Paleozoic and Mesozoic rocks are obliquely thrust southwards over Cenozoic rocks along the Kabateh section of the Rudbar Fault, which represents a strong structural and topographic boundary (Figure 2). Further east, the Rudbar Fault cuts across the Sefid Rud, continuing up the northern forested slopes of Kūh-e Āsemān Sarā, which forms an elevated outlier of Paleozoic and Jurassic units, before eventually dying out in Cenozoic units within the foothills north of the Shahroud River. The Manjil thrust lies 10 km south of the Rudbar Fault, and displaces Paleozoic and Early Cenozoic units over Late Cenozoic (Neogene) sediments flanking the Alborz range front.

A sharp step in the Moho exists in the vicinity of the Rudbar and Manjil Faults, decreasing northwards from ~50 to ~35 km, as revealed by receiver function studies of the West Alborz (Rahmani et al., 2019; Teknik et al., 2019). The Rudbar fault is therefore located in a region of sharp contrast in continental lithospheric strength.
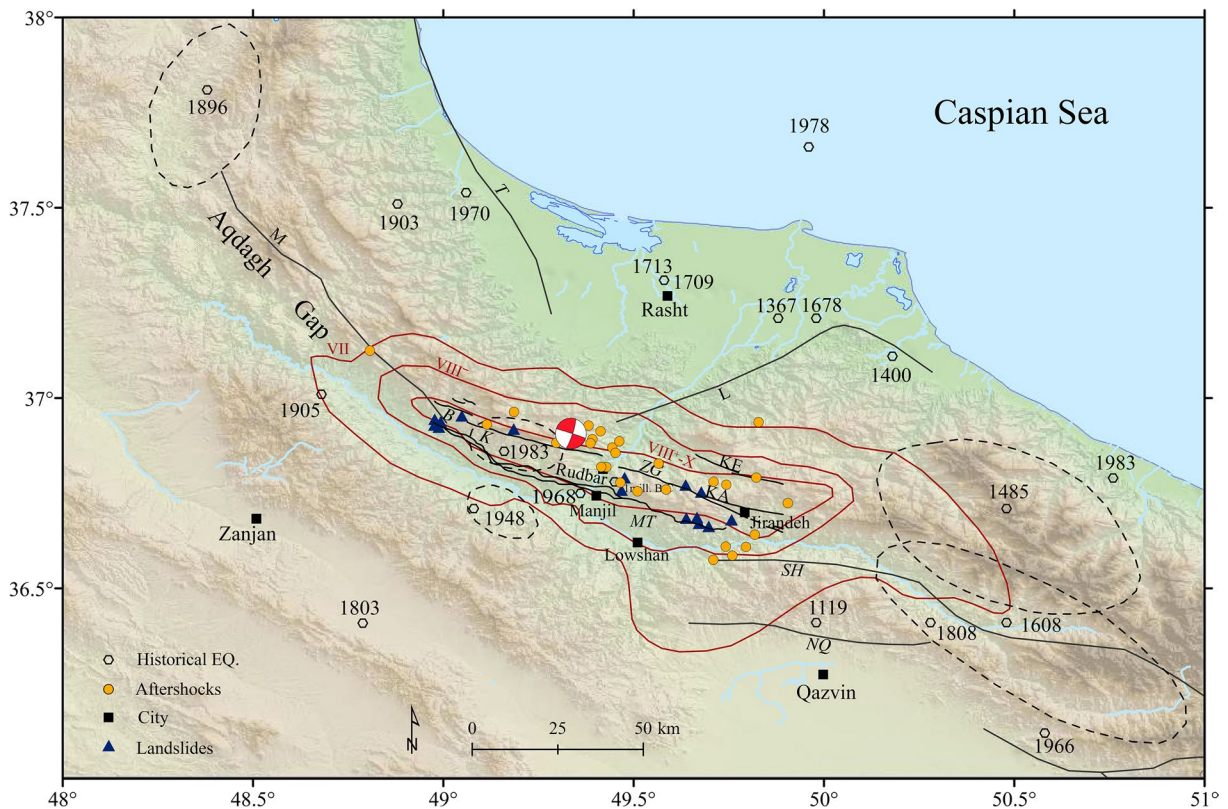
Figure 3. The black solid lines present the Rudbar fault trace mapped by Berberian et al. (1992); other faults are reported by Berberian and Walker (2010) and Hessami et al. (2003). Letters indicate various faults: B (Baklor), K (Kabateh), KA (Kashachal), KE (Kelishom), L (Lahijan), M (Masuleh), MT (Manjil Thrust), NQ (North Qazvin), SH (Shahrud), T (Talesh), and ZG (Zard Geli). The mainshock is shown by the red focal mechanism (Gao & Wallace, 1995). The location of the mainshock and aftershocks (Orange circles) are from (https://www.sciencebase.gov/catalog/item/5de542cae4b02caea0e8fa90). Blue triangles show landslides documented throughout the region (Berberian & Walker, 2010). Red closed lines denote MMI isoseismal contours (Berberian et al., 1992). The black dash polygons shows the approximate affected regions of large historical events (Berberian et al., 1992), Black hexagons show various historical earthquakes (Ambraseys & Melville, 2005; Berberian, 1983; Berberian et al, 1983, 1992; Berberian & Qorashi, 1984).

Quaternary activity along the Rudbar Fault suggests it is a relatively immature structure, producing limited features in the geomorphology that survive erosion in this dynamic mountain environment. Prior to the 1990 earthquake, the Rudbar Fault had not been recognized or mapped, and consequently its significance to the seismic hazard of the region was unknown (Berberian & Walker, 2010).

2.2. 1990 Rudbar Earthquake

The West Alborz is seismically active and prior to the 1990 Rudbar earthquake, a number of destructive earthquakes were known from both historical and modern times (Figure 1c; for further discussion, see Ambraseys & Melville, 2005; Berberian & Walker, 2010). Historical earthquakes in the Rudbar region include the 1485 Upper Polrud earthquake (Ms 7.2), and 1608 Alamutrud earthquake (Ms 7.6), which both occurred east of the Rudbar epicenter (Figure 3; Ambraseys & Melville, 2005; Berberian & Walker, 2010). Only a few moderate magnitude events have been recorded instrumentally prior to the Rudbar earthquake (Berberian, 1983; Berberian & Walker, 2010; Jackson et al., 2002). The Rudbar earthquake happened within the eastern part of the Rudbar-Aqdagh gap, which separates the epicentral regions of the 1485 and 1608 earthquakes in the east from the 1896 Khalkhal-Sangrud earthquake (Ms 6.7) in the northwest (black dash polygons in Figure 3). Therefore, a better understanding of the Rudbar earthquake is important for improved characterization of the seismic potential of the western (Aqdagh) part of the seismic gap (Berberian et al., 1992).

The June 20, 1990 Rudbar earthquake represents the largest known event to have affected this region, killing ~15,000 people, and leaving a further 500,000 homeless (Berberian & Walker, 2010). The economic infrastructure of Gilan and Zanjan provinces were both severely affected, while the direct economic cost of the earthquake has been estimated at ~2.5% of GDP. The Rudbar earthquake thus represents one of the worst natural disasters to have affected Iran in recent times.

Berberian et al. (1992) mapped a 80 km coseismic surface rupture associated with three fault segments, west-to-east: Baklor, Kabateh, and Zard Geli, which together comprise the Rudbar Fault (Figure 1c; Berberian et al., 1992). The three segments are arranged in a right stepping en-echelon pattern with a strike of 95°N–120°N on near-vertical planes (Berberian et al., 1992). Field measurements of coseismic fault slip revealed oblique slip, with up to ~1 m left-lateral and vertical (thrust) slip (north-directed) on both the Kabateh and Zard Geli segments (Figure 1c; Berberian & Walker, 2010; and references therein). Seismic Modified Mercalli Intensity (MMI) (Berberian et al., 1992) was generally well correlated with the fault rupture region, albeit extending marginally north of the fault along the southeast section of the Zard Geli segment (in the vicinity of the Kelishom fault, see Figure 3).

Different epicenter locations are reported by different agencies and studies (summarized in Berberian & Walker, 2010). The EHB catalog locates the epicenter at 37.00°N and 49.22°E (International Seismological Center, EHB Bulletin, http://www.isc.ac.uk, International Seismological Centre, United Kingdom, 2009). Gao and Wallace (1995) and Engdahl et al. (2006) relocated the epicenter to 36.96°N 49.34°E, and 36.99°N 49.22°E, respectively. Despite the difference of a few kilometers between epicenters, they both lie ~10 km north of the coseismic rupture mapped in the field. This discrepancy could easily result from bias in the earthquake locations, which are based on teleseismic data (e.g., Ghods et al., 2012; Aziz Zanjani et al, 2013). However, the relocation of the Rudbar earthquake cluster improved the location of the epicenter to 36.91°N 49.34°E (https://www.sciencebase.gov/catalog/item/5de542cae4b02caea0e8fa90). The epicenter of the Rudbar mainshock lies along the western section of the Kebateh segment, suggesting a mostly eastward-propagating rupture. Body-waveform modeling of the earthquake reveals a left-lateral focal mechanism, consistent with (1) several aftershocks located along-strike (Gao & Wallace, 1995), (2) the Rudbar Fault structure, as mapped in the bedrock geology (Hessami et al., 2003), and (3) field mapping of the surface ruptures (Berberian et al., 1992). The relatively low double couple (56%) in the NEIC W-phase solution (see https://earthquake.usgs.gov/earthquakes/eventpage/usp0004arq/moment-tensor), coupled with various peaks in the source time function highlight the complexity of the earthquake source. Using P and SH body waves, Campos et al., (1994) modeled the source as a sequence of nine sub-events (Table 2—see also Section 5.2 for additional discussion). The earthquake initiated with a low moment sub-event, and for the first 10 s following the ISC onset time the moment release could not be resolved. The first major sub-event (#1 of Campos et al., 1994) occurred at 10 s, and was located along the central Kabateh segment (marking the onset of the mainshock). The rupture then propagated bilaterally at ~2.5 km/s for the next 10 s, at which point the rupture terminated to the west (~20 km west of the epicenter). However, toward the east, the rupture experienced a sharp increase in the moment release rate (at 20 s), with enhanced slip in two major sub-events (#6 and #7 of Campos et al., 1994), located 30–40 km east of the epicenter (and east of Sefid Rud). The rupture continued to propagate unilaterally toward the southeast before terminating ~60 km from the epicenter. The main difference between a simple point source approximation and more complex source models therefore involves the modeling of large sub-events east of the epicenter. The preferred solution of Campos et al. (1994), which involved nine sub-events, a sub-fault rupture duration of Ts = 6 s, and average rupture velocity of 2.5 km/s, gave the most coherent set of focal mechanisms along the fault, and a 32% reduction in the RMS error compared with a single point source approximation. The three main sub-events (#1, #6, and #7) accounted for 50%–60% of the total moment release (Table 5 of Campos et al., 1994). Using a similar approach, albeit with a slightly higher bandwidth and based only on P waves, Choy and Zedník (1997) obtained similar results to Campos et al., (1994). However, by increasing the resolution of the source functions for the various sub-events, Choy and Zedník (1997) were able to resolve (slightly) finer detail on the rupture geometry and relative locations between sub-events.

Choy and Zedník (1997) argued that the aftershock locations (derived from teleseismic data; see Gao & Wallace, 1995) were likely to be collectively relatively robust, despite substantial bias affecting individual locations. In the first 3 h following the mainshock, most of the aftershock activity was focused close to

Table 1
Specifications of Images Used in This Study

	Pre-earthquake				Post-earthquake					
	KH-9	SPOT		Aerial photo		SPOT				Aerial photo	Sentinel-2A
Time	September 2, 1980	July 24, 1989	July 29, 1989	1955–1956	1968	April 21, 1994	October 9, 1994	October 18, 1994	August 26, 1996	2001–03	September 8, 2018
Type	Frame camera	push broom	push broom	Frame camera	Frame camera	Push broom	Push broom	Push broom	Push broom	Frame camera	Push broom
Resolution (m)	6–9	10	10	1–3	1–3	10	10	10	10	1–3	10
Focal length (cm)	30.5			154.34	152.57					153.24	

the fault rupture, gradually expanding during the first 24 h (Choy & Zedník, 1997). However, over the following 3 months activity around the rupture zone diminished, while aftershocks appeared to migrate northwards, clustering around Sefid Rud and the hanging-wall region of the Khazar Fault. Although this northward spread of the aftershock cloud might be impacted by location bias from the rather sparse and uneven distribution of seismic networks in 1990, the co-existence of distributed left-lateral and thrust focal mechanisms might also indicate activation of a complex network of faults similar to that observed for the Varzeghan-Ahar, 2012 event (Ghods et al., 2015). Nevertheless, the NEIC mainshock epicenter was located ~10 km north of the mapped surface rupture, which broke a near vertical fault plane; this suggests a northward bias for earthquake locations in this region at this time (Berberian et al., 1992).

A key conclusion from both seismology (Choy & Zedník, 1997) and field-based (Berberian et al., 1992) studies of the Rudbar earthquake is that each fault segment (Baklor, Kabateh, and Zard Geli) ruptured as discontinuous en echelon fault segments. Therefore, the failure of an asperity must be communicated to a neighboring asperity either by (1) connection of the two asperities at depth, or (2) stresses are readily transmitted through the intervening volume, while each segment remains unconnected. The main goals of this paper are thus to investigate the surface rupture of the Rudbar earthquake using current optical geodesy techniques, and reconcile these new observations with those from seismology.

3. Optical Image Processing

Optical Image Correlation (OIC) of historical aerial photos and modern satellite images provides important constraints on the near-field surface displacement associated with coseismic fault ruptures. OIC processing tools, such as COSI-Corr (Leprince et al., 2007), ASP (Beyer et al., 2018), and MicMac (Rosu et al., 2015), can be used to retrieve continuous 2D maps of on-and off-fault surface deformation (e.g., Barnhart et al., 2020; Milliner et al., 2016, 2015; Socquet et al., 2019; Vallage et al., 2016; Zinke et al., 2019, 2014). OIC has limited decorrelation near the fault rupture and thus can overcome the near-field limitations of InSAR, which typically decorrelates in high-strain regions close to fault ruptures. Furthermore, OIC is the only geodetic technique able to retrieve dense maps of ground deformation associated with earthquakes prior to the era of modern satellite geodesy (pre ~1992). To determine the near-field surface displacement associated with the Rudbar earthquake, we apply OIC to various satellite and aerial photo datasets, as discussed below.

3.1. SPOT Satellite Data

We use COSI-Corr (an IDL software package for the Coregistration of Optically Sensed Images and Correlation) to investigate the magnitude and distribution of coseismic ground displacement from SPOT 10 m satellite images (Leprince et al., 2007; COSI-Corr: available for free download from http://www.tectonics.caltech.edu/slip_history/spot_coseis/index.html/)—see Table 1. SPOT satellite images cover a large area (60 km by 60 km), so the majority of the epicentral region can be imaged by a single scene, thus allowing a

regional view of the earthquake displacement field. However, this comes at the cost of reduced precision for the displacement values, and lower spatial detail (compared with correlation of higher resolution images, such as aerial photos, see Section 3.2). We first orthorectify and co-register the SPOT images using an external digital elevation model (DEM), with referencing information coming from the satellite metadata (which was found to be well-registered to the Earth's surface). Orthoimages are then correlated using sub-pixel phase correlation, which gives east-west and north-south displacement maps (Leprince et al., 2007). Optical images must first be resampled into a common viewing geometry to be able to isolate meaningful signals associated with coseismic displacement between two images; during this process, we also co-register the two images and correct for topographic distortion (orthorectification). Therefore, OIC yields displacement maps in the horizontal plane. To retrieve a 2D horizontal displacement map, we need only one pair of images spanning the earthquake. Unlike InSAR techniques, which are sensitive to land surface changes over short periods of time, OIC can give robust measurements of ground deformation from images separated by many years (e.g., Zhou et al., 2016).

For the SPOT data used in this study, we follow the 3D processing workflow of Zinke et al., (2019) to determine the 3D displacement field produced by the Rudbar earthquake. Despite vertical displacements reported in the field (Berberian et al., 1992) we do not see any significant displacement in the north-south or vertical components, because the earthquake was largely strike-slip. Nevertheless, the 3D processing approach helps to reduce topographically correlated noise in the east-west component, which would otherwise be present due to the typically large east-west perpendicular baselines between the limited number of SPOT acquisitions covering this area. To obtain the 3D displacement map, we process two images acquired before the earthquake and two images after the event, with different (stereoscopic) viewing geometries needed to isolate the pre-and post-earthquake stereoscopic (i.e., noise) component. We then orthorectify, coregister and correlate three moving images (one pre-earthquake and two post-earthquake images, Table 1) relative to a pre-earthquake reference image (chosen based on the incidence angle closest to nadir). We use a multi-scale sliding window to compute the horizontal displacement field for each combination of reference and moving images, yielding three displacement maps. To minimize mis-registration between the orthorectified images, resulting from sensor parameters and topography, we refine our co-registration by optimizing the various match points used to link images, while also accounting for sensor characteristics and topography. To remove medium-and long-wavelength topographic signals, we orthorectify images using 30 m resolution ALOS AWD3D World DEM. The correlation map between pre-earthquake pairs contains only the stereoscopic component of the pre-earthquake topography, while the pre-post correlation maps contain the earthquake-related displacement and a combination of pre and post-earthquake topographic signals (the post-topography can be isolated from both pre-post correlations; see also Avouac & Leprince, 2015; Zinke et al., 2019). In the next step, we compute the 3D deformation field using the three 2D correlation maps, which must be aligned and sampled onto the same grid. At each pixel location, we compute four sight vectors, which connect the position of the satellite in space during sensing of this particular pixel (determined from the satellite metadata), and the ground position of the pixel (given by the georeferencing of the displacement maps). Because any uncorrected stereoscopic effects will manifest as an apparent displacement (which will be the case if the same DEM is used to orthorectify the pre-and post-earthquake image), we can compute the true position of the pixel from the point of nearest intersection between the pre-earthquake sight vectors and the post-earthquake sight vectors. The 3D displacement is given by the difference in the pre- and post-earthquake triangulated XYZ positions for each pixel (in ECEF [Earth-Centered, Earth-Fixed] coordinates). We need to apply several steps to reduce sensor artifacts and spurious values from the 3D displacement maps. We remove outliers in each displacement map by applying a noise filter based on neighborhood statistics (see Zinke et al., 2019). Pixels with values highly dissimilar to their neighbors are replaced by null values. We remove a ramp estimated from values located far from the surface rupture, where displacements are expected to be zero. We discard values with a low signal-to-noise ratio (SNR). Parallel stripes and undulations caused by CCD mis-alignments are removed using the destriping tool in COSI-Corr, which subtracts the average background striping values estimated from non-deforming parts of the displacement map. Finally, we apply a 3 × 3 pixel-wide median filter to further reduce outliers and smooth values (Leprince et al., 2007).

3.2. Air Photos and KH9 Images

To increase the signal-to-noise ratio in the displacement measurements, as well as the spatial detail that we can resolve, we correlate higher resolution KH-9 satellite (6–8 m) and aerial images (1 m), which are processed using a new workflow based on the Ames Stereo Pipeline (ASP) image processing suite developed by NASA (Beyer et al., 2018; Broxton & Edwards, 2008; Shean et al., 2016). In both cases, we use ASP to register the images to the Earth's surface using ground control points, GCPs collected from an independent reference image and DEM, for example, Landsat-8 or GoogleEarth, and AWD3D DEM. A minimum of three GCPs are required to solve for the camera pose, although we generally collect up to ~15 to obtain a more robust solution (distributed evenly across the image, and collected from relatively flat regions to minimize elevation errors). The GCPs allow us to solve for an approximate starting camera, which is subsequently refined in the stereo processing; in this way we mitigate registration problems that may arise from using post-event images to register pre-event images. We then automatically generate match points linking all available stereo images, which are then used in a bundle adjustment procedure to refine the camera parameters (e.g., pose, distortion parameters, etc), before computing stereo disparities, triangulating the ground position at each pixel, and finally resampling onto a regular grid to produce a high-resolution DEM. This procedure is repeated for both pre- and post-earthquake datasets. We then use the high-resolution DEMs and refined camera parameters to orthorectify the raw images. For large aerial photo networks, we also mosaic the component aerial orthoimages to make a regional-scale orthomosaic, which significantly simplifies the final correlation step. This step requires high quality registration between all images within the network, which can be achieved through bundle adjustment. We obtain the final high resolution displacement field by correlating pre- and post-earthquake orthomosaics using phase correlation. Because we have access to the pre- and post-earthquake DEMs, we are able to remove the majority of stereoscopic noise present in the aerial photos during the final orthorectification step.

Several challenges must be overcome when processing aerial photos. First, we must pre-process the photos: rotating and cropping each image to a common image size. Because we often lack the metadata required to process aerial photos for high-precision geodetic purposes, we first need to estimate the true position of the camera for each image, the orientation of the camera in space, as well as any lens distortions, and principal point offsets. Fortunately, we know the starting focal length and dimensions of the image plane (estimated from fiducial positions coupled with knowledge of the scanning resolution), and using GCPs we can estimate the camera pose in a projected coordinate system. Remaining camera parameters (i.e., camera intrinsics) can be estimated and refined during bundle adjustment, which minimizes the intersection error between triangulated rays at matched pixel locations (linking two or more images) projected by their respective cameras into 3D space. We apply Tsai's calibration algorithm (Tsai, 1987) to initialize the camera pose for each image. This approach assumes only a first order radial distortion for the camera. Since errors in the camera position and orientation, as well as distortion, can strongly influence the accuracy of the final DEM, we then refine the parameters of each camera using bundle adjustment, which considers triangulated match points in the optimization, and ensures that observations of a single ground feature are self-consistent across multiple images. We select match points (i.e., tie points) based on feature matching techniques (e.g., SIFT, or OBAloG), which locates common pixels in the overlapping region of neighboring images. A feature of ASP which can significantly improve the quality of the stereo matching procedure is to first mapproject the images with a low resolution DEM, which in turn removes the long-wavelength stereoscopic component, thus simplifying the subsequent correlation procedure. The low resolution DEM is then accounted for during the final triangulation process, before rasterizing the final point cloud to give a high resolution DEM. This procedure can help to improve the quality of the stereo disparities, and thus the final DEM, particularly when using the block correlator approach in topographically rough regions (initial mapprojection of images is less important when using semi-global matching approaches). DEMs are generated for each overlapping stereo pair (typically images with 60% stereo overlap), which are then mosaiced together using a blending technique to generate a seamless final DEM.

Any errors in the camera pose which were not corrected during bundle adjustment will result in a final DEM which is misaligned to the Earth's surface (or a good quality reference DEM); this is quite common, as bundle adjustment attempts to solve a highly non-linear problem with many free parameters. Fortunately, ASP has several tools to address these issues. One powerful approach is to find a global transformation that
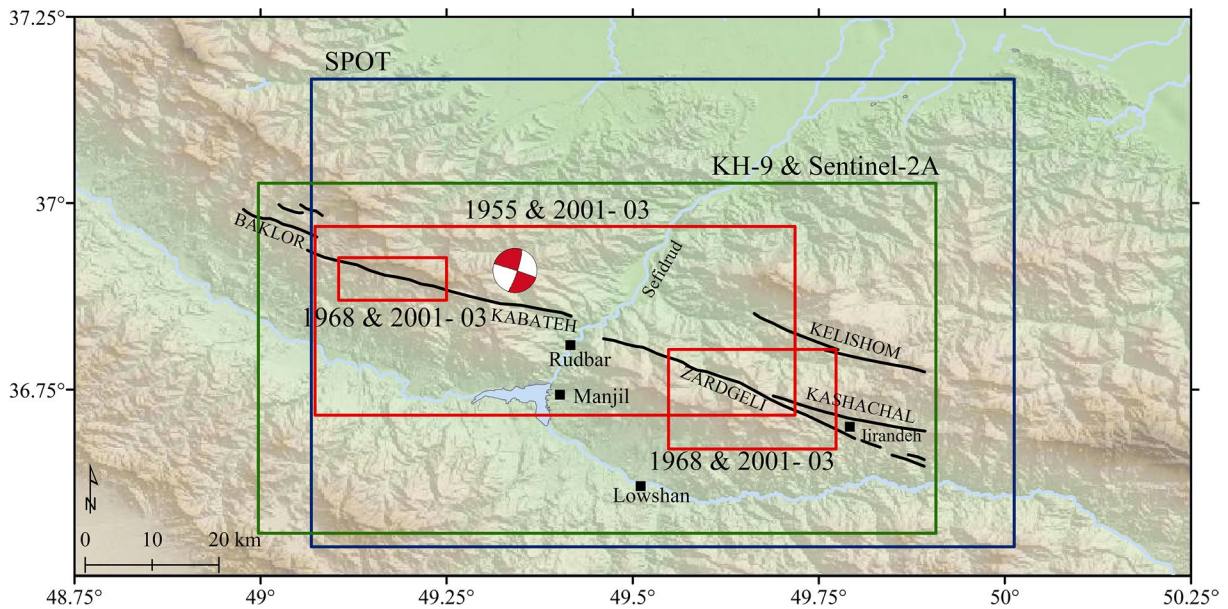
Figure 4. Coverage map for the various optical datasets overlapping area used in this study, shown with rectangles. SPOT imagery (blue), KH9 and Sentinel-2A (green), 1955–2001/3 aerial photos (red), and 1968–2001/3 aerial photos (dashed red). Black solid lines show faults in the region of study (Berberian & Walker, 2010). Black squares show the approximate location of the cities.

brings the final DEM into close alignment with a reference DEM. This is important for subsequent image processing, as mis-registrations between datasets can corrupt the final displacement estimates. We use an Iterative Closest Point (ICP) algorithm (Pomerleau et al., 2013), implemented in ASP, to determine this global transform, which is then applied to the final DEM and the corresponding cameras (i.e., updating the pose for each camera). To further refine cameras to eliminate small registration problems that may remain between images, and/or to further improve the distortion model we apply a second bundle adjustment (optional weighting of the camera pose will force the optimization to refine the distortion parameters). This then requires a second iteration of stereo-matching, DEM generation, orthorectification, and mosaicing. ASP also has an option to use a reference DEM as an additional constraint in the bundle adjustment process. For this to work, one needs to have the disparity maps of the raw input images, and the cameras must already be well-registered to the reference DEM, which is then used to generate GCPs. During optimization, each GCP is projected into the left and right camera, and the difference in pixel positions are compared to the raw image disparity map computed at those two pixel locations. When cameras are very well-aligned to the reference topography, the difference in pixel positions for each GCP should agree well with the raw image disparity maps. Once we have generated well-registered DEMs and high quality orthomosaics, we then correlate orthomosaics which bracket the earthquake in time. Additional post-processing of the resulting displacement map is needed to remove outliers. The final output is a high resolution 2D displacement map. Vertical displacements may also be retrieved either from DEM differencing (which is a reasonable approximation when the topography is smooth), or by differencing height values while accounting for the horizontal displacement (more accurate). This is important, because if rough topography has been translated horizontally, one will subtract the height at different positions on the topography, resulting in residual topographic noise (e.g., Oskin et al, 2012). In the case of the Rudbar earthquake, the displacement is largely horizontal, and mostly related to high frequency variability in the fault strike, so we do not report the vertical displacements here.

4. Results

4.1. Correlation of SPOT Images

We measure the displacement field associated with the Rudbar earthquake using eight panchromatic SPOT 10 m satellite images (Figure 4) spanning eight years from 1989 to 1996 (Table 1), and covering ~71 km
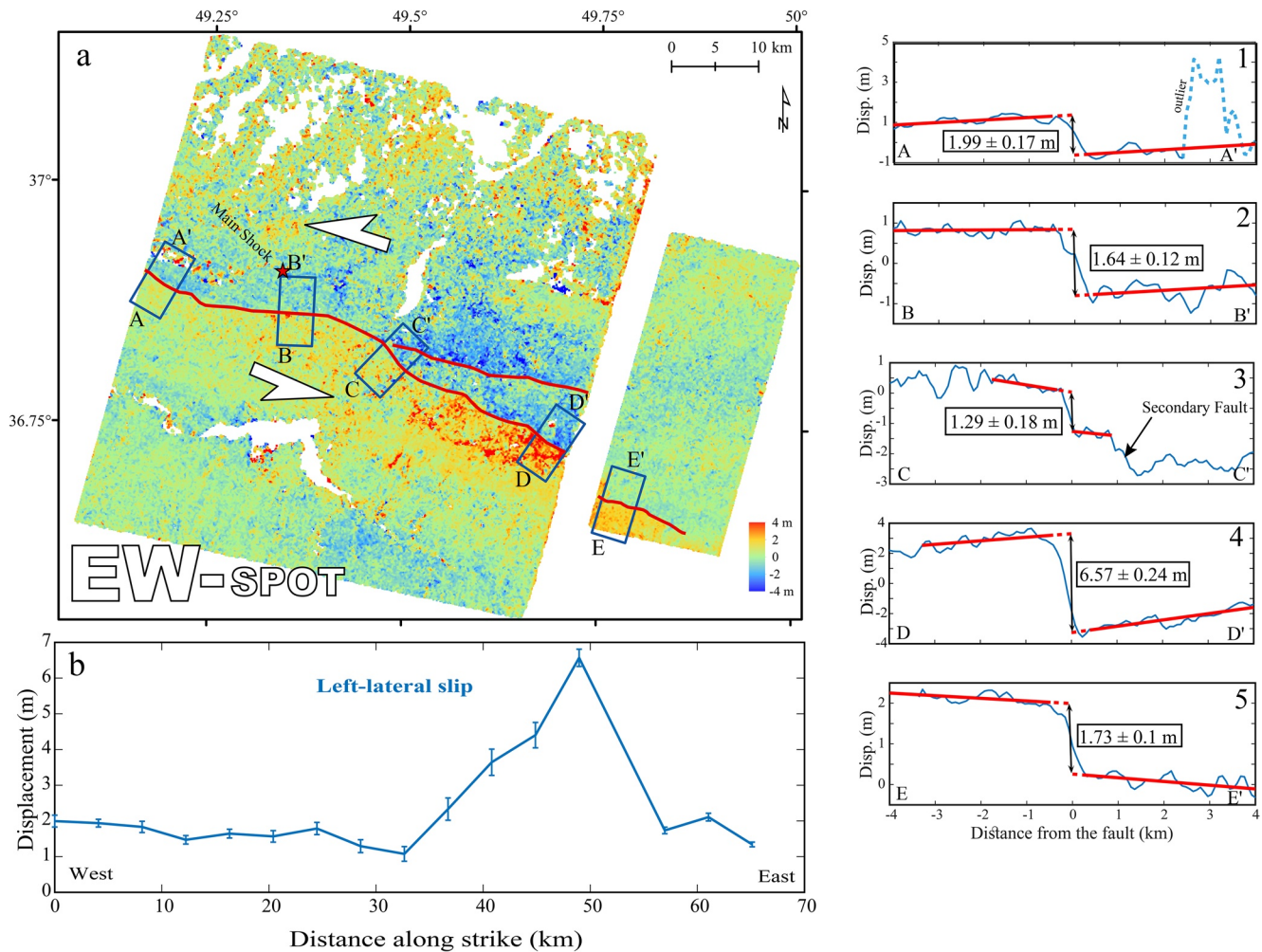
Figure 5. Ground displacement field obtained from SPOT images. (a) East-west displacement map. Red solid lines are the rupture traces extracted from optical image correlation (OIC) of SPOT images. The red star indicates the epicenter of the mainshock and the blue rectangles are stacked profiles illustrating offset in the fault parallel (left-lateral) direction. Profiles (1)–(5) show displacements within 4 km wide swaths along profiles AA′, BB′, CC′, DD′, and EE′. (b) shows slip distribution along Rudbar rupture trace obtained from OIC of SPOT images. Vertical bars represent error in displacement measurement for each swath profile. The start and end points are located in 36.89°N, 49.19°E and 36.65°N, 49.85°E, respectively.

of the rupture mapped by Berberian et al., (1992). These images cover the center and eastern part of the Rudbar fault, namely Kabateh and Zard Geli segments (Baklor segment is not covered). Figure 5a shows the east-west (EW) displacement map obtained following the procedure described in section 3.1. We use the SPOT image acquired on the July 24, 1989 as a reference image and correlate it with the three other images, acquired on July 29, 1989, April 21, 1994 and October 9, 1994. All of these images cover the center part of the rupture. To investigate the eastern part of the rupture, we add four other SPOT images acquired on July 24, 1989 (reference image), July 29, 1989, September 18, 1994, and August 26, 1996 (moving images). We use a correlation window size of 64×64 to 32×32 pixels, with a step distance of eight pixels (80 m), with frequency masking enabled to suppress high frequency noise (e.g., Ayoub et al., 2009; Leprince et al., 2007).

We measure the total co-seismic displacement along the Rudbar surface rupture using stacked profiles perpendicular to the fault strike (blue rectangles in Figure 5a). We stack the displacement profiles (over 4 km) to increase the signal-to-noise ratio of the displacements (the profiles extend ± 4 km perpendicular to the fault rupture). Five strike-slip displacement profiles are shown in Figure 5 (AA′, BB′, CC′, DD′, and EE′). Figure 5b shows an average fault parallel displacement of ~2.3 m using all the stacked perpendicular profiles along the fault. The minimum and maximum offsets are 1.08 ± 0.2 m, which is located ~16 km east of the epicenter, and 6.57 ± 0.24 m, located ~30.5 km east of the epicenter, respectively (Figures 5a

and 5b). (All reported errors given henceforth represent the standard deviation of the linear trend used to estimate the displacement each side of the fault; it is also important to note that these error estimates do not include uncertainty associated with the interpretive nature of choosing which parts of the profile we use to estimate the linear trends each side of the fault—noise significantly impacts these interpretations. All profiles and interpretations are presented in Supplementary Material). Between profiles CC′ and DD′, the fault rupture can be seen to splay onto two fault segments. The southern most of these is consistent with the field mapping of Berberian et al., (1992). However, the northernmost segment, which appears to represent an eastward continuation of the Kabateh segment east of Sefid Rud, was not mapped following the earthquake. Figure 10a also shows this secondary fault rupture, from correlation of SPOT photos. The average left lateral strike slip displacement over a stacked profile of 20 km width and 4 km length (profile 1, Figure 10), indicates ∼1.2 m displacement along this secondary rupture. However, the fault zone width (FZW) is noticeably broader, with lower slip than the Zard Geli segment to the south. This structure runs along an active river channel, which likely contributes to the highly distributed surface rupture, evidenced by the smooth displacement profile across the fault. Alternatively, slip along this segment may simply have been blind, and not reached the surface.

4.2. Correlation of Aerial Photos

Aerial photos cover the western part of the Rudbar fault better than the SPOT images (Figure 4), while also providing more spatial detail and higher precision on the fault displacements. We follow the method described in section 3.2 to make high resolution orthomosaics spanning the Rudbar rupture. The various data sets include three subsets of images covering 1955–56 (45 photos), 1968 (49 photos), and 2001–2003 (39 photos) (Table 1). Although the 1955–56 photo coverage is good (Figure 4, solid red rectangle), the southeastern part of the rupture is not covered, and the time between pre and post collections is about 44 years (one of the longest documented epochs for an OIC study). We therefore complement the 1955–56 photos with images from 1968, and these are then both correlated with post-event images from 2001–2003, thereby giving a more comprehensive coverage of the entire rupture zone. We compare the results from different multi-scale correlation window sizes, using orthomosaics resampled over a range of resolutions (1 –5 m) to find the optimum parameters which (1) minimizes areas of poor correlation (typically given by small windows), (2) minimizes smoothing (large windows), and (3) maximizes spatial detail (smaller windows). Our final correlations use a multi-scale sliding window size from 256×256 to a final window size of 32×32, with a step of eight pixels, and images resampled at 1 m (1968–2003) and 3 m (1955–2003). Figures 6a and 7a show the east-west displacement maps obtained from the 1968–2003 correlation for Kabateh and Zard Geli segments, respectively (Figure 4, red dash rectangles). Blue rectangles in both correlation maps (Figures 6a and 7a) indicate stacked profiles oriented perpendicular to the fault rupture (0.4 km wide by 1.2 or 1.6 km long). Stacked profiles showing the fault-parallel (i.e., left-lateral) displacement for Kabateh and Zard Geli are shown in Figure 6a (profiles 1–4) and 7a (profiles 1–4). Figures 6b and 7b show the slip distribution along Rudbar fault rupture (field measurements are shown as yellow dots). The minimum and maximum left-lateral displacements for Kabateh are about 0.62 ± 0.05 m and 2.42 ± 0.05 m, located 15.75 and 13.4 km west of the epicenter, respectively (Figures 4 and 6). For the Zard Geli segment, the minimum and maximum offsets are 2.16 ± 0.11 m and 5.79 ± 0.92 m, located 23.1 and 33.8 km east of the epicenter, respectively.

We correlate 1955 aerial photos with 2001–2003 post-event photos, which provide better coverage of the study area (red rectangle in Figure 4). Figure 8a shows the whole correlation map obtained using a multiscale sliding window (initial size: 256×256, and final size: 32×32). Despite dense vegetation east of Sefid Rud, and the long temporal interval of 46–48 years, the images correlate well, and we could trace the rupture along much of Kabateh and Zard Geli segments (Figure 8a). Stacked fault parallel displacement profiles (0.48 km by 1.2, 2.4, or 4.8 km) are shown in Figure 8, profiles 1–3 (Kabateh segment) and Figure 8, profiles 4–5 (Zard Geli segment). The minimum and maximum displacements for Kabateh are 0.43 ± 0.19 m and 3.29 ± 0.25 m, located ∼1.2 km east and ∼19.3 km west of the epicenter, respectively. The minimum and maximum offset for Zard Geli are 1.25 ± 0.23 m and 5.6 ± 0.27 m, located ∼20.8 and ∼29.9 km east of the epicenter, respectively. The left-lateral slip distributions for both Kabateh and Zard Geli segments are shown in Figures 8b and 8c. Figures 8a and 10b also shows the east-west displacement map from 1955 and 2001–2003, which covers the continuation of the Kabateh segment east of Sefid Rud. The
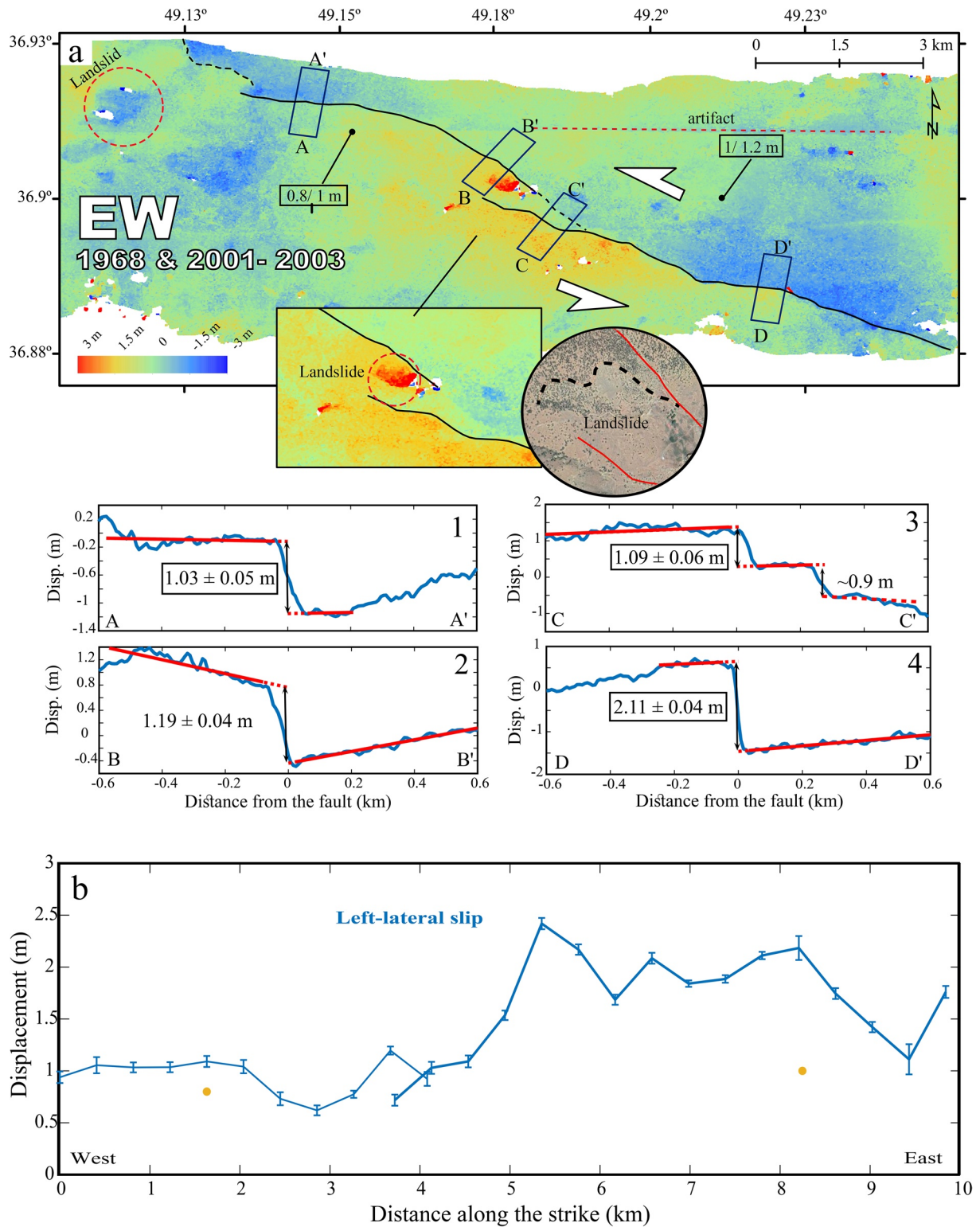
Figure 6. (a) East-west displacement map for the Kabateh segment. Black solid lines show the rupture trace; black dash lines shows the fault trace with less certainty. The blue rectangles show the location of stacked profiles, several of which are presented in 1–4. The red dash circles are landslides, the red dash line indicates the artifact in optical image correlation. The horizontal/vertical field displacements are given in black boxes (Berberian & Walker, 2010). The circle inset map indicates a landslide visible in the step-over near profile BB′ (2). (1)–(4) show fault parallel displacements within 0.4 km wide swaths along with profiles AA′, BB′, CC′, and DD′. (b) shows the left-lateral slip distribution along the Kabateh segment. Yellow dots in (b) show horizontal field displacements (Berberian & Walker, 2010).
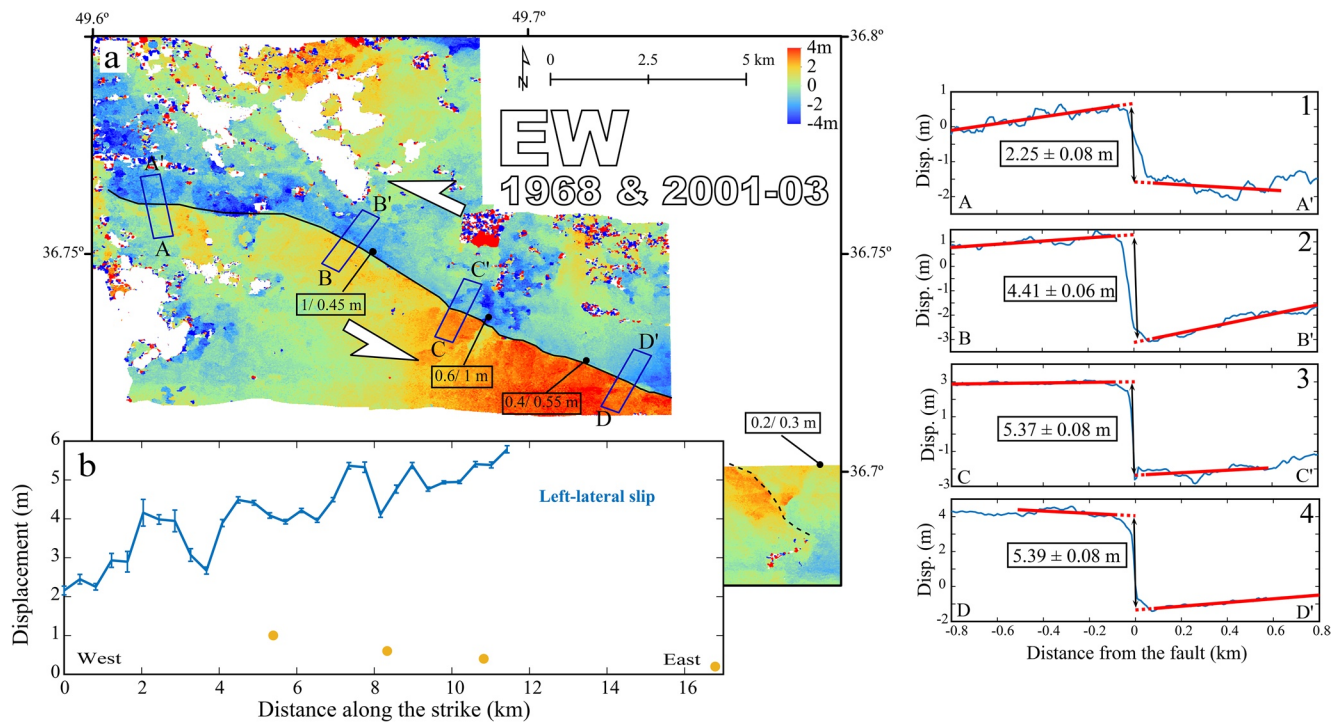
Figure 7. (a) East-west displacement map for the Zard Geli segment, from correlation of 1968 and 2001–2003 aerial photos. Black solid line is the rupture traces from correlation of the 1968–2003 aerial photos. Black dash line shows the trace of fault obtained from correlation of SPOT images. Blue rectangles are stacked profile locations (0.4 km wide). Horizontal/vertical filed displacements are given in black boxes (Berberian & Walker, 2010). (1)–(4) show fault parallel displacements profiles from the blue boxes (corresponding to profiles AA′, BB′, CC′, and DD′). (b) Left-lateral slip distribution along the Rudbar rupture trace obtained from correlation of aerial photos, Yellow dots show horizontal field displacements (Berberian & Walker, 2010).

average left-lateral displacement along this segment is ~1.75 m (Figure 10, profiles 2 and 3, using a stack width of 6 km by 1.2 km length).

4.3. Correlation of KH9 Photos

We orthorectify a KH-9 image (acquired on September 2, 1980; see Table 1) using ASP, as described in section 3.2. We then correlate the pre-event KH-9 orthoimage with a post-event Sentinel-2A image (band 3) acquired on 8th September 2018 (chosen to minimize the seasonal difference in illumination conditions, e.g., Marchandon et al., 2018). We use a multi-scale sliding window (256 × 256 to 32 × 32 pixels), with a step of eight pixels, yielding a final ground sampling of 40 m. Figure 9a shows the east-west displacement map. Despite dense vegetation across the region, the long temporal interval between pre- and post-event images (38 years), and the presence of clouds on KH-9 image close to the rupture which results in decorrelation (white areas in Figure 9a), we could trace the rupture along most of the Kabateh segment and all of the Zard Geli segment. Stacked displacement profiles across the fault (2 km wide by 8 km long) are shown in Figure 9a, profiles 1–2 (Kabateh), and profiles 3–4 (Zard Geli). Figures 9b and 9c show the along-strike left-lateral displacement for both segments, based on the stacked profiles. The minimum and maximum displacement for Kabateh is 0.79 ± 0.14 m and 3.62 ± 0.21 m, located 9 and 19.9 km west of the epicenter, respectively. The minimum and maximum displacement for Zard Geli is 1.04 ± 0.66 m and 5.89 ± 0.36 m, located 15.7 and 30.3 km east of the epicenter, respectively.

5. Discussion

5.1. New Constraints on Near-Field Surface Slip From Optical Correlation

We develop a new workflow (based on ASP and the phase correlator of COSI-Corr) for extracting dense measurements of ground displacement resulting from the 1990 Rudbar earthquake, using historic optical
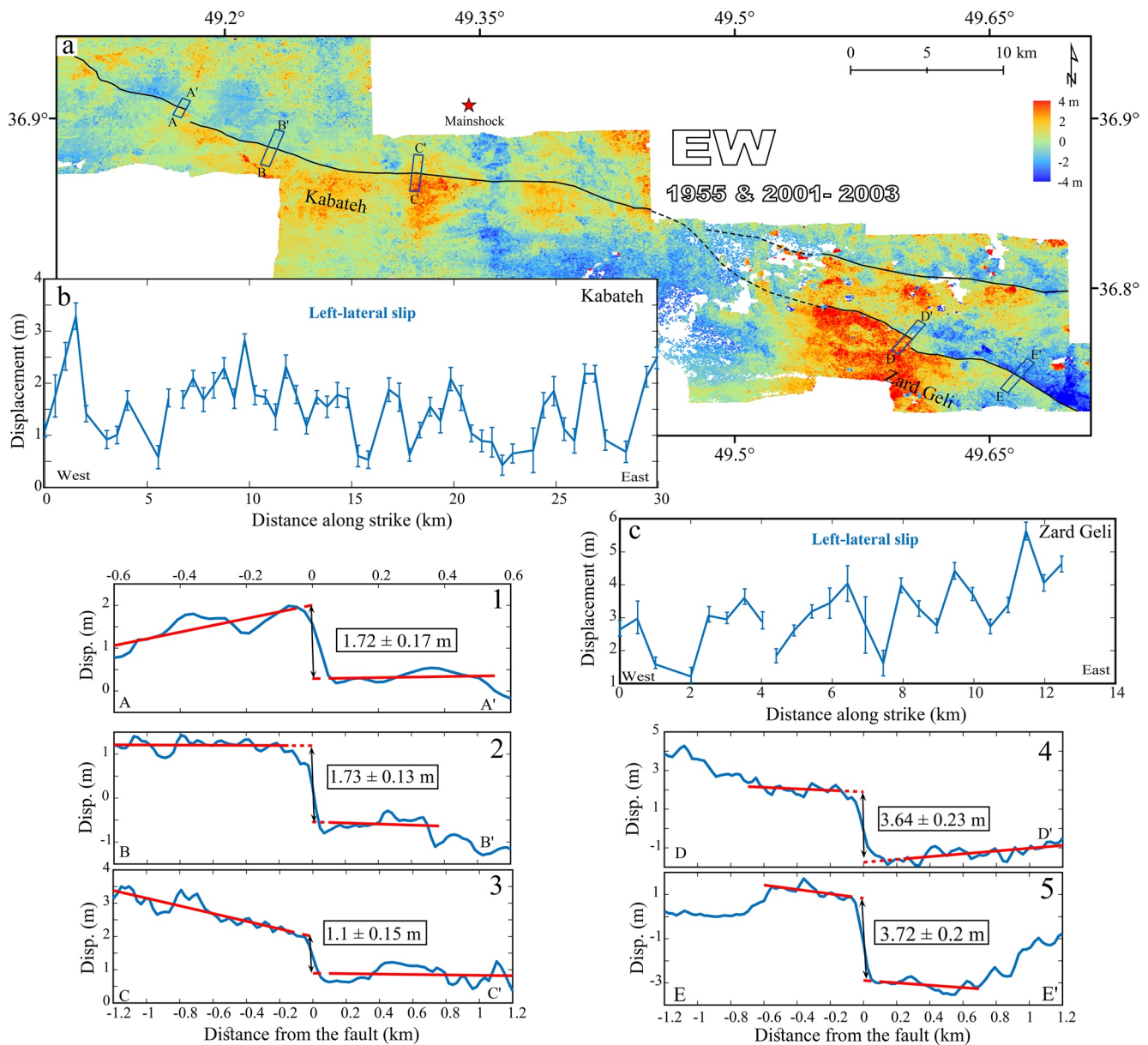
Figure 8. (a) East-west displacement map for the Kabateh and NW Zard Geli segment from correlation of 1955 and 2001–2003 aerial photos. Black solid lines are the rupture traces from the 1955 and 2001–2003 aerial photos, black dash line show fault obtained from correlation of SPOT images. The blue rectangles are stacked profiles presenting offset in fault parallel direction. (1)–(3) are displacements within 0.48 km wide swaths along with profiles AA′, BB′, and CC′, for Kabateh segment. (4) and (5) are displacements within 0.48 km wide swaths along with profiles DD′ and EE′ belongs to Zard Geli segments. (b) and (c) shows left-lateral slip distribution along Rudbar rupture trace obtained from the correlation of the aerial photos.

aerial and satellite imagery. Despite the long time interval between pre- and post-earthquake image acquisitions (spanning the Rudbar event), poorly constrained initial camera parameters, rough topography, and dense vegetation, we show that our workflow can resolve the horizontal surface deformation field with an accuracy of 1/10th of the input image pixel resolution, thus providing new constraints for this and potentially many other recent historical earthquakes predating the era of modern space-born geodesy (e.g., InSAR and GPS, i.e., ~1992 onwards).

We measure an average displacement of ~220 cm along ~71 km of the Rudbar rupture. Inclusion of data from the low slip Baklor segment (western termination of the rupture), which was not well documented by our available data (meaning we miss ~9 km of the rupture), would reduce the average slip. Our results are in
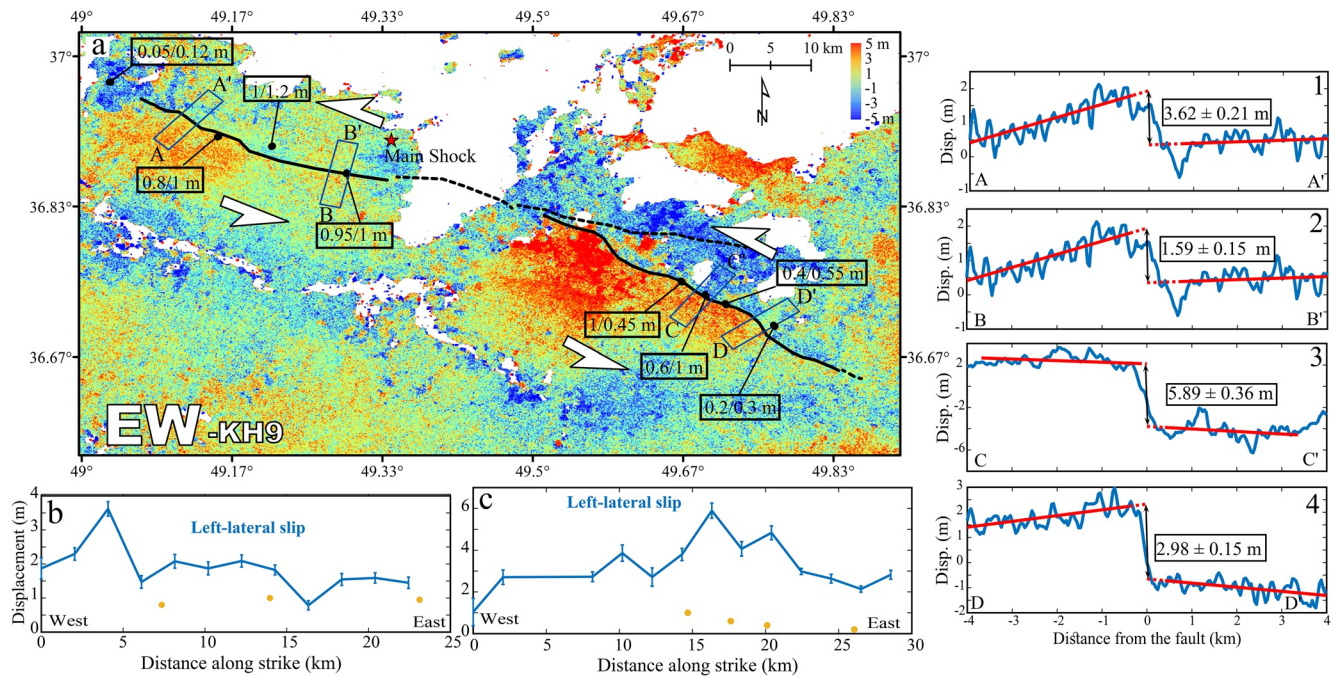
Figure 9. (a) East-west displacement map from the correlation of KH9 and Sentinel-2A satellite images. Black solid lines show the rupture trace based on the displacement map; black dash lines show fault trace from correlation of SPOT images. The red star indicates the epicenter and blue rectangles are stacked profiles presenting offset in fault parallel direction. Horizontal/vertical field displacements are given in black boxes (Berberian & Walker, 2010). (1) and (2) are displacements within two km wide swaths along profiles AA′ and BB′ along Kabateh. (3) and (4) are displacements within two km wide swaths along profiles CC′ and DD′ along Zard Geli. (b) and (c) shows left-lateral slip distribution along Rudbar rupture trace obtained from the correlation of KH9 and Sentinel-2A images for two segments. Yellow dots show horizontal field displacements (Berberian & Walker, 2010).

good agreement with the strike-slip focal mechanism of Berberian et al. (1992) and Gao and Wallace (1995). Average surface displacements measured from our correlation data are also in very close agreement with the expected average displacement (i.e., ∼240 cm) assuming a rupture plane of 15 km (down-dip width) by 80 km (along-strike length; e.g., Berberian et al., 1992 and Berberian & Walker, 2010), a rigidity of 30 GPa, and a seismic moment of ∼8.8e + 19 Nm (Gao & Wallace, 1995). Our results therefore explain a long-term paradox regarding the Rudbar earthquake, whereby field observations of surface slip were unusually low given the large seismic moment release in the mainshock.

Using a dense temporary seismic network deployed 8 years after the mainshock, Tatar and Hatzfeld (2009) investigated the local seismicity along the eastern segment of the Rudbar fault for a seven week period. Based on the maximum focal depths of well-located events, they suggested a maximum depth of 20 km for the Rudbar rupture plane. However, a width of 20 km for the Rudbar fault requires an average displacement of ∼183 cm, which is smaller than our surface estimate of ∼220 cm. The average surface slip of continental strike-slip earthquakes is generally equal or less than the average slip for the whole rupture plane (e.g., Fialko et al., 2005; Xu et al., 2016). Therefore, the maximum depth of seismicity reported by Tatar and Hatzfeld (2009) is likely to represent an upper-bound, given that significant aftershock diffusion will have occurred in the 8 years following the mainshock (Das & Henry, 2003).

5.2. Spatial Variation in Along-Strike Slip

The distribution of surface slip along the fault is shown in Figures 11a and 11b (SPOT data only) and Figure 12a (all data sets). A significant peak in left-lateral slip of ∼6 m is located ∼40 km east of the epicenter, along the Zard Geli segment (∼20 km east of Rudbar town, and ∼8 km west of Jirandeh, Figure 1c). The displacements near Rudbar and Jirandeh are both about two meters, which likely accounts for the high number of fatalities in these towns: 2691/16.6% (Rudbar) and 1776/9% (Jirandeh), see "Presidency Islamic Republic of Iran Plan and Budget Organization," (https://www.mporg.ir). The gradual increase in slip
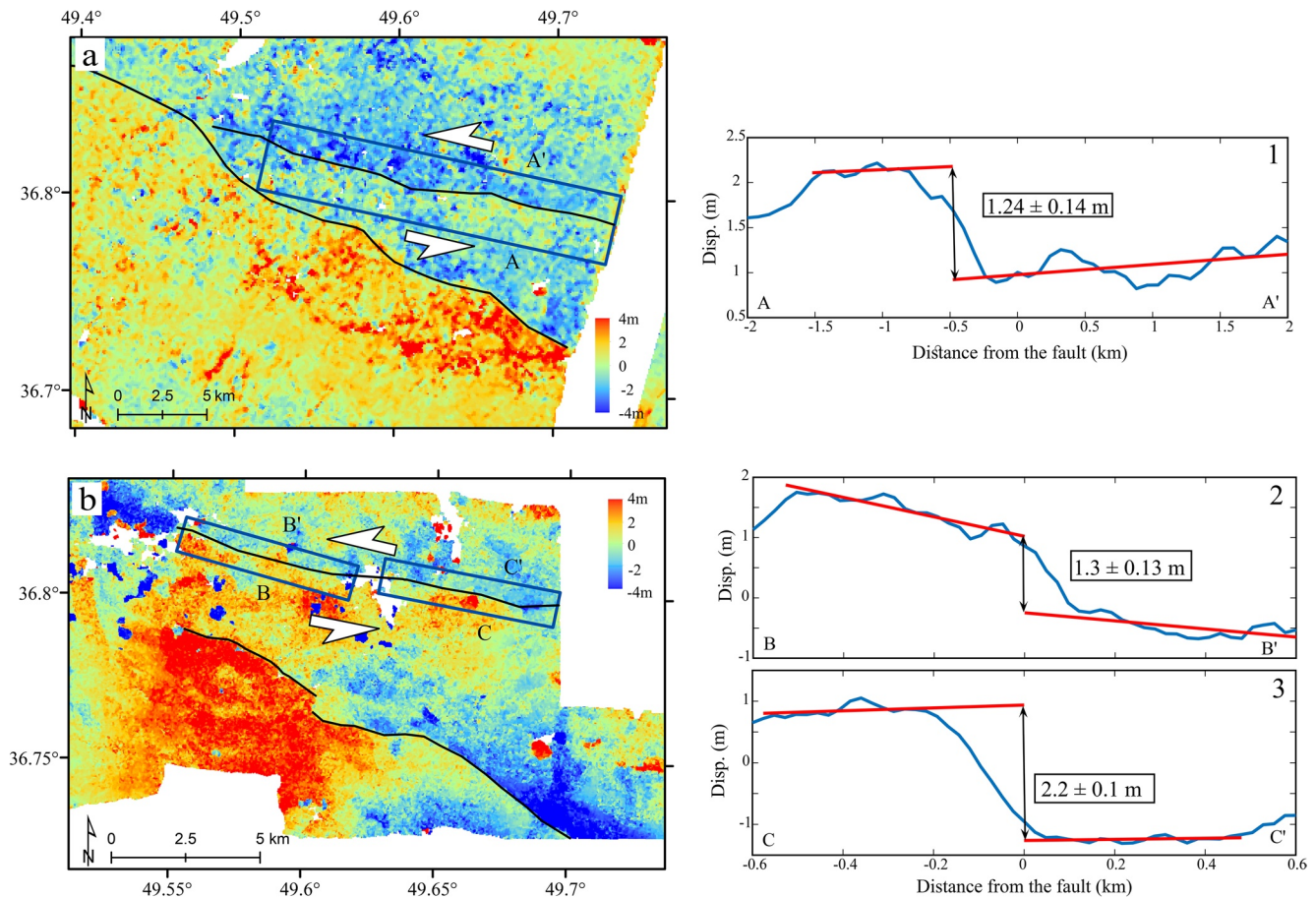
Figure 10. (a) East-west displacement map of SPOT images. Zard Geli and the secondary Hajideh fault ruptures are shown in black. (1) is fault parallel displacement within 20 km wide swath along profile AA′. (b) East-west displacement map from correlation of 1955 and 2001–2003 aerial photos. (2) and (3) are east-west displacements within 6 km wide swaths along profiles BB′ and CC′.

toward the east is consistent with the widening of the macroseismic isoseismal intensities (Figure 3; see Berberian et al., 1992).

The along-strike slip distributions obtained from OIC (i.e. Figures 5b, 6b, 7b, 8b and 8c, 9b and 9c) are all in relatively good agreement with the along-strike displacement inferred from the inverted multi-source model of Campos et al. (1994) (Table 2), from the inversion of body waves (Figures 11c). The maximum slip from their model (i.e., peak moment release) is ~6 m, located about 45 km east of the ISC epicenter, while a second peak of ~4 m is located 65 km to the east, and correlates with the maximum surface displacements from OIC. This high slip section corresponds to the Zard Geli fault segment, which broke east of Sefid Rud.

Figures 11b and 12b show the along-strike fault-normal slip, which is generally much lower than the strike-slip component (consistent with the source properties of the earthquake). Despite the low signal-to-noise ratio for this component, small fluctuations in fault geometry (Figure 11e) can be seen to correlate strongly with the along-strike variability in fault-normal slip (Figure 11b), as well as the long-term topography (Figure 11f). Fault geometry likely plays an important role in controlling the long-term evolution of fault slip, particularly the vertical component which will be well-expressed in the topography. Fault-normal slip is both compressional (positive values) and tensional (negative values); the rapid change between modes can be achieved by small fluctuations in dip on a near-vertical strike-slip fault. The pattern of fault-normal slip does not appear to correlate with left-lateral slip (Figures 11a and 11b, and Figures 12a and 12b). The peak compressional fault-normal slip (thrust) is located at the junction between the Kabateh and Zard Geli fault segments (co-located with Sefid Rud), which also features the largest number of thrust aftershocks (Figure 1c). Interestingly, the regions of compression correlate with low topography, while regions of extension
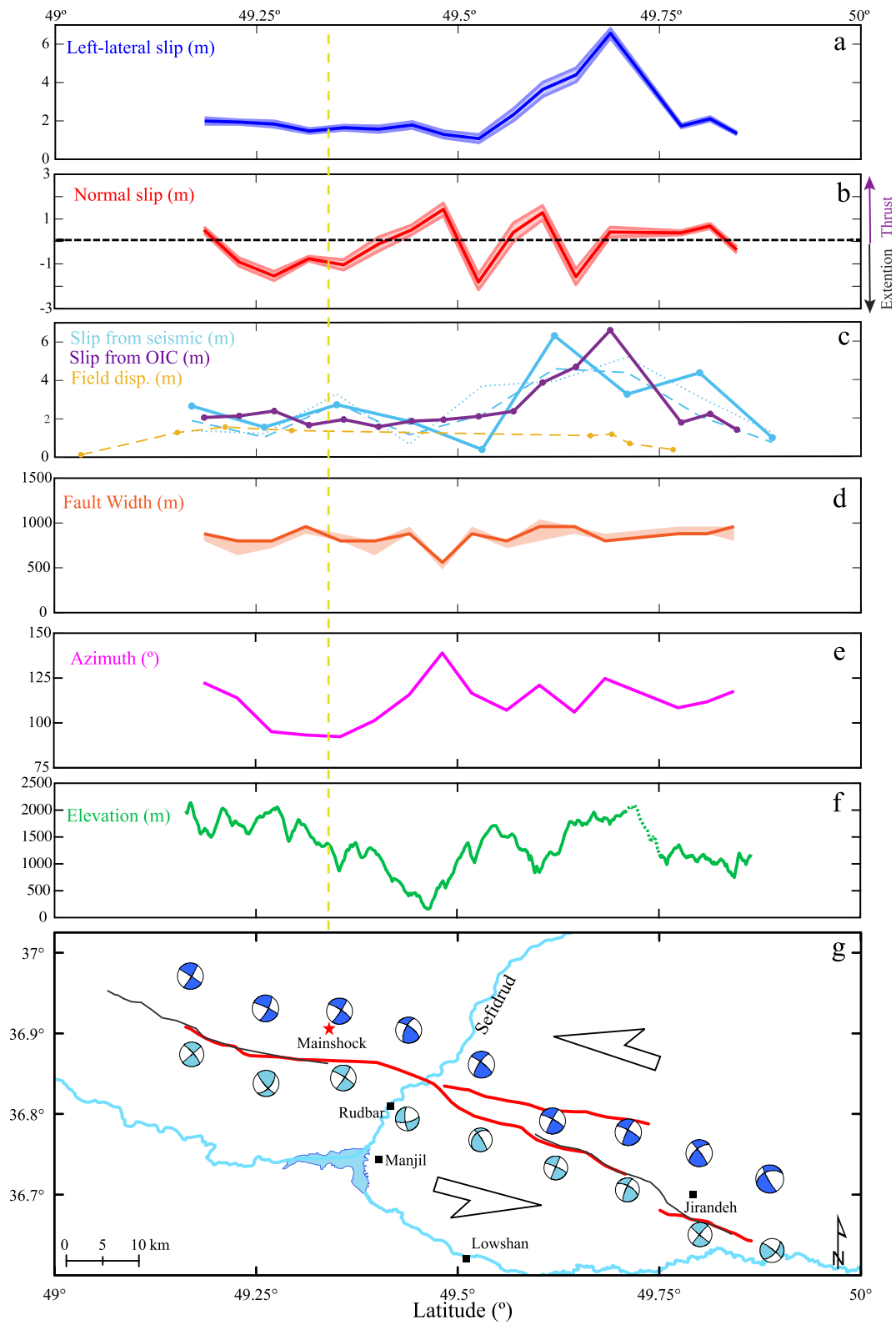
Figure 11

correlate with high topography (Figures 11b and 11f). However, we note that the fault-normal component estimated from SPOT data (Figures 11b) is at the limit of resolution (~1/10th pixel, i.e. ± 1 m), and shows some inconsistencies with higher-resolution estimates from aerial photo data (Figure 12b), particularly for the Zard Geli segment, which is located in very rough topography. It is likely that topographically correlated noise from stereoscopic residuals and illumination bias (Lacroix et al., 2019) impacts the SPOT displacements at the sub-pixel scale.

Figure 11g shows the geometry of the Rudbar fault rupture, along-side the multi-source focal mechanisms of Campos et al (1994) based on a 4 s (light blue) or 6 s (dark blue) rupture time for each 10 km fault patch. The focal mechanisms are highly consistent with the mapped fault rupture (red line in Figure 11a); small variations in strike correlate well with geometric complexities along the fault. Slip was predominantly left-lateral strike-slip (Figures 11a and 12a), and was relatively uniform, 1–2 m, along the Kabateh segment, increasing dramatically to ~6 m along the Zard Geli segment, before dying out over the next ~15 km where the rupture terminated just after a major bend in the fault 3 km east of Jirandeh.

Based on the modeling of Campos et al (1994), the mainshock likely initiated on the central (east-west striking) Kabateh segment, before propagating bilaterally to the west and east. To the west, at 49.25°E, the rupture changed strike from westward to northwest propagating (Figure 11e), before terminating in a region of increasing topography dissected by deeply incised rivers (Figure 13). However, as the rupture propagated to the east, it was not arrested by the deviating fault strike into the Sefid Rud river valley, which also represents a major negative topographic feature crossing the fault. One possible explanation the rupture was able to propagate across this feature may lie in the reduced normal stress associated with this topographic low, which may have promoted slip more than the geometric complexity hindered it. Nevertheless, the rupture then propagated eastward on two different structures. The majority of slip was partitioned onto the Zard Geli segment (1.5–6 m), which was unknown prior to the earthquake, and represents a geometrically more complex structure than the (here named) Hajideh fault to the north (blue fault in Figure 13), which accommodated a smaller amount of distributed left-lateral slip (1–2 m) over a distance of ~23 km (Figure 10).

The Hajideh segment appears to be structurally continuous across the Sefid Rud, linking with the eastern Kabateh segment. Furthermore, it strikes eastward with a relatively straight geometry along a river valley, continuing up into the high Alborz, and along a fault trace which appears to have a stronger signal in the long-term topography than the Zard Geli segment (Figure 13). It is therefore unclear why the rupture died out on this structure, while propagating instead to the southeast along the Zard Geli segment, which (1) is structurally more complex, (2) strikes across steeper topography, and (3) shows a more subdued signal in the long-term topography. More puzzling is the dramatic increase in moment release on this structure (Campos et al., 1994), which slipped up to ~6 m as it ruptured across elevations of ~2000 m. One explanation may be that the Hajideh fault broke historically more recently than Zard Geli, and so the latter was more critically stressed prior to the earthquake (e.g., Schwartz et al., 2012). The same may also be true for the neighboring the Kelishom and Kashachal faults, which lie east of the Hajideh fault, and which did not slip during the Rudbar earthquake. The positive Coulomb stress change induced on Zard Geli by ~1.8 m of left-lateral slip on Kabateh may have been enough to bring it to failure (Figure 14).

Field investigation along the Hajideh fault revealed no obvious surface ruptures, similar to where the rupture crosses the Sefid Rud (Manuel Berberian, pers. comm., 2020). However, the long-wavelength offset across this structure (Figure 10, profiles 1–3), which is accommodated across a zone up to ~1 km wide, suggests either that the rupture did not propagate all the way to the surface, and/or some of the surface slip was highly distributed, perhaps in response to the weak sedimentary materials through which they broke. Lacking any evidence of surface rupture based on field surveys, this structure was not previously considered

Figure 11. (a) Left- lateral (blue), and (b) fault-normal (red) slip profile plotted along-strike by latitude. Solid lines are the total displacement over a four km swath, error bars reflect uncertainty in the linear regressions used to determine the fault offset. (c) Total slip from seismic moments of sub-events (light blue solid, dashed, and dotted lines associated with 4, 6, and 10s, respectively) obtained from body wave modeling (Campos et al., 1994), total displacement from optical image correlation (violet) and horizontal field displacement (yellow) (Berberian & Walker, 2010). Sub-event distances are with respect to the mainshock epicenter at 36.908°N and 49.3436°E, from (https://www.sciencebase.gov/catalog/item/5de542cae4b02caea0e8fa90). (d) Fault zone width (orange), (e) Fault-strike azimuth, and (f) Topography, plotted along-strike of the Rudbar rupture. (g) Location of the mapped fault obtained from correlation of SPOT images. Red star is the mainshock location. Light and dark blue focal mechanisms belong to sub-events for rupture duration of 4 and 6 s, respectively (Campos et al., 1994). Yellow dashed line (a)–(f) shows the longitude of the mainshock epicenter.
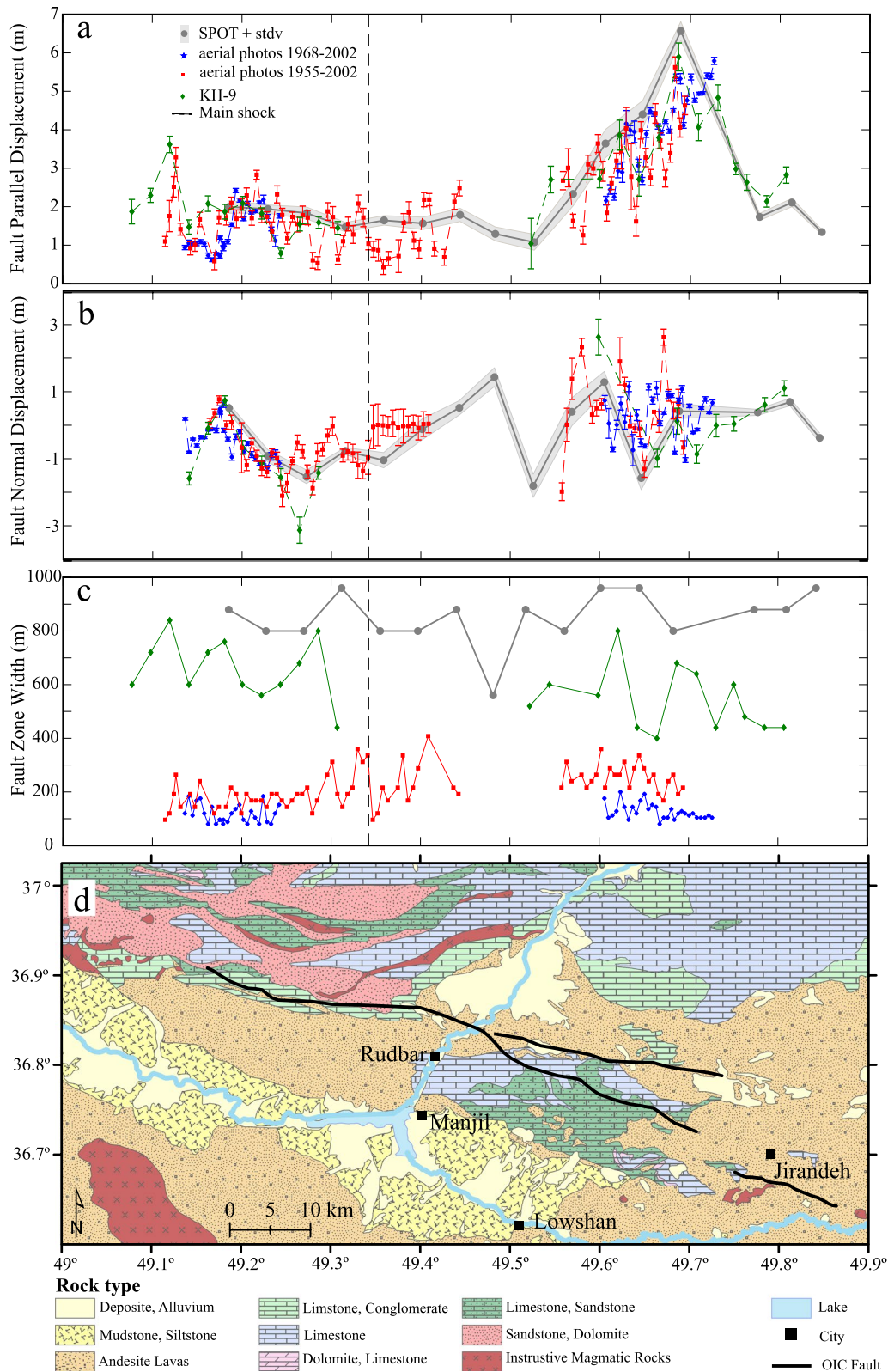
Figure 12. (a) Fault parallel, and (b) normal offset along the longitude of the mapped Rudbar fault based on correlation of SPOT images (gray dots), aerial photos (red and blue symbols, with their standard deviation), and KH9-Sentinel-2A images (green symbols). The mainshock longitude is marked by black dashed line. Gray area shows the standard deviation of the SPOT displacements. (c) Fault zone width estimated for the Rudbar fault rupture, based on correlation of the various images. (d) Geological map of the Rudbar earthquake area.

Table 2
Focal Parameters and Seismic Moments (M_0) of Sub-events Obtained From Body Wave Modeling Ts = 4 s (Campos et al., 1994)

Sub-event	$d^{(a)}$ (km)	$Az^{(b)}$ (degree)	$T_b^{(c)}$ (sec)	$T_s^{(d)}$ (sec)	Strike (degree)	Dip (degree)	Slip (degree)	H (km)	$M_0 \times 10^{19}$ (N.m)	Disp. (m)
3	−20	300.0	8.0	4	318.8	89.3	−1.7	8.4	1.60	2.66
2	−10	300.0	4.0	4	319.5	102.7	−31.8	9.5	0.93	1.55
1	0	0	0	4	302.4	77.8	−6.3	14.3	1.63	2.72
4	10	120.0	4.0	4	258.1	111.6	18.2	7.1	1.11	1.85
5	20	120.0	8.0	4	327.8	80.4	55.1	19.1	0.23	0.38
6	30	120.0	12.0	4	293.8	81.6	2.3	9.8	3.78	6.3
7	40	120.0	16.0	4	300.2	63.6	13.9	3.7	1.95	3.25
8	50	120.0	20.0	4	310.6	94.8	3.9	6.5	2.62	4.36
9	60	120.0	24.0	4	308.8	83.0	153.0	14.5	0.59	0.98

(a) Distances with Respect to the Mainshock Epicenter on 36.99°N and 49.35°E Based on the ISC Catalog (International Seismological Center, ISC Bulletin, http://www.isc.ac.uk, Internatl. Seis. Cent., United Kingdom, 2009), Negative and Positive Values Present West and East of the Epicenter, Respectively. (b) Rupture Direction. (c) Time Delay with Respect to the Epicenter. (d) Time of Rupture Duration. H Indicate the Sub-events depth.

in any seismological investigation of this earthquake. Nevertheless, the various displacement fields from optical correlation suggests that slip was relatively continuous (at least at shallow depths) between the various fault segments comprising the Rudbar rupture (although there is still some ambiguity in the aerial photo correlation data covering Sefid Rud, which is impacted by dense vegetation, strong topographically correlated signals, and landsliding).

Although we do not document the vertical displacements along the rupture, due to substantial topographic residuals in our DEM differencing results, field measurements indicated a significant average vertical
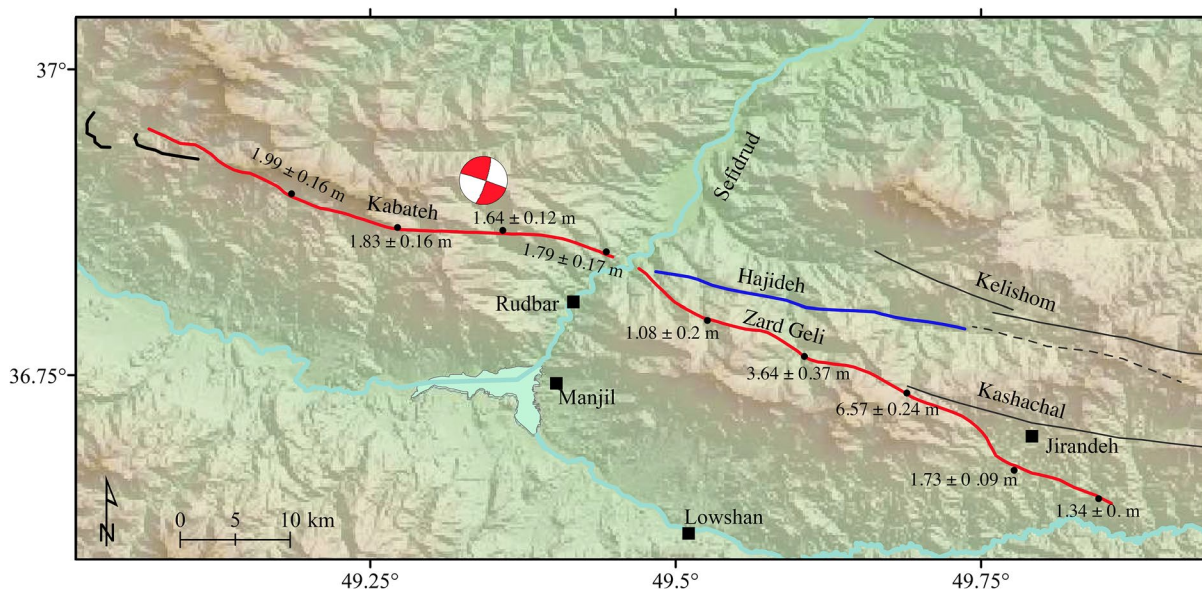

Figure 13. Details of the final mapped fault trace retrieved from optical image correlation. The red line shows both Kabateh and Zard Geli segments of the Rudbar fault, west and east of Sefi Rud, respectively. The blue solid line shows the secondary Hajideh fault, and the black solid lines indicates small segments of Baklor segment. The gray solid lines shows Kelishom and Kashachal faults (Berberian & Walker, 2010) The red focal mechanisms shows the location of the mainshock. Black points indicated left-lateral displacement measurements on SPOT correlation maps, every 8 km. Black squares show the approximate location of cities.
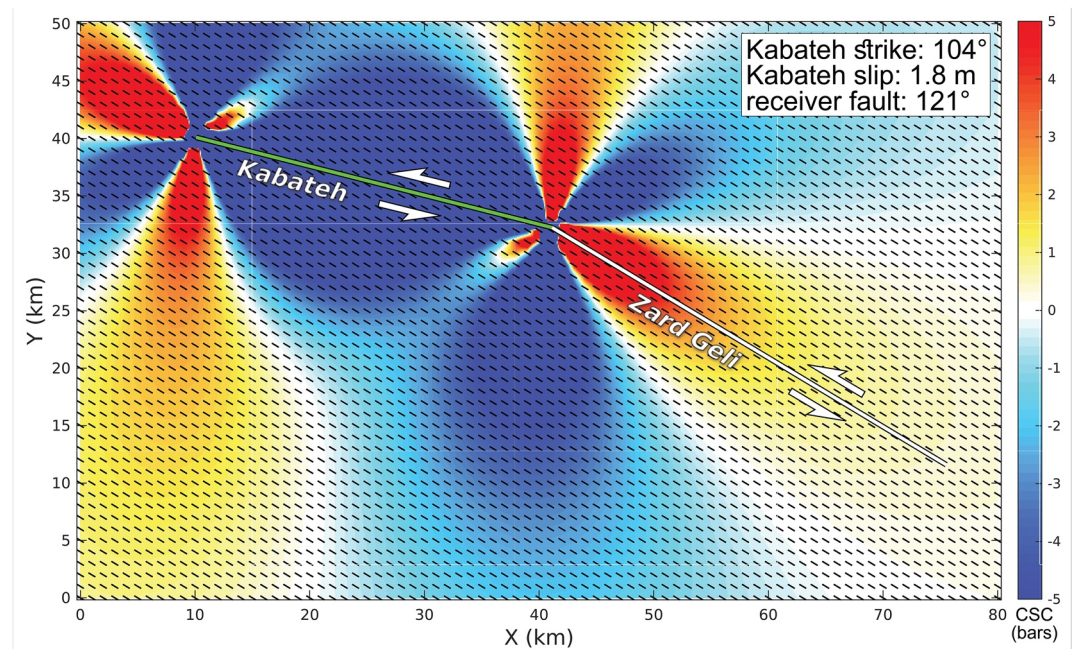
Figure 14. Coulomb stress change calculation for the Kabateh fault, using a slip of 1.8 m, and receiver faults of 121° (i.e., the strike of Zard Geli).

displacement of ∼95 cm along the fault, in contrast with the pure strike-slip sense of motion from the main-shock focal mechanism (Gao et al., 1991; Thio et al., 1990). A possible explanation for this discrepancy may be that some of this signal reflects apparent vertical motion associated with a translation of topography in a mountainous region, or uplift due to local geometric variability along-strike and local gravitational effects.

5.3. Off-Fault Deformation (OFD)

It has long been known that a proportion of coseismic slip is accommodated by inelastic processes in the volume surrounding a fault plane (i.e., the damage zone), e.g., Chester and Chester (1998), Rockwell et al. (2002), Mitchell and Faulkner (2009). A notable feature of the 1990 Rudbar earthquake was the surprisingly small surface displacements mapped along the rupture for the size of the earthquake (Berberian et al., 1992). Field measurements indicated oblique slip (left-lateral and thrust motion) of up to ∼1 m at sites located on Kabateh and Zard Geli (Berberian & Walker, 2010). However, OIC estimates indicate left lateral slip of up to ∼6 m along the fault. Figure 11c shows how field measurements compare with OIC estimates of fault slip from SPOT data, and seismology data.

Field measurements typically represent spatially hyper-localized estimates of on-fault slip, whereas OIC allows one to capture both the on- and off-fault components of slip accommodated over wider regions, extending several hundred meters around the fault (e.g., Milliner et al., 2015; Zinke et al., 2019). Therefore, a simple calculation of the difference between OIC and field estimates of fault slip can help to isolate the OFD component of slip (assuming this difference is of tectonic origin, and the field measurements are representative of the real surface slip localization). If the OIC estimates of fault slip represent the total deformation accommodated across the entire fault zone (primary fault core + damage zone), then OFD can be expressed as a percentage of the total (i.e., OIC) slip. Figure 15a presents estimates of OFD for various field sites along the rupture. The amount of OFD is generally high along the Rudbar rupture: 20%–50% along Kabateh segment, and 70%–90% along Zard Geli segment.

In the event that there is no OFD, then the low field displacements imply a dramatic drop in moment release near the surface (e.g., "shallow slip deficit, SSD," see Fialko et al., 2005), which has been proposed for other strike-slip earthquakes, although not for such an extreme drop in moment. The degree of SSD has also been proposed to scale with structural maturity of a fault, a proxy for which is the cumulative geological offset
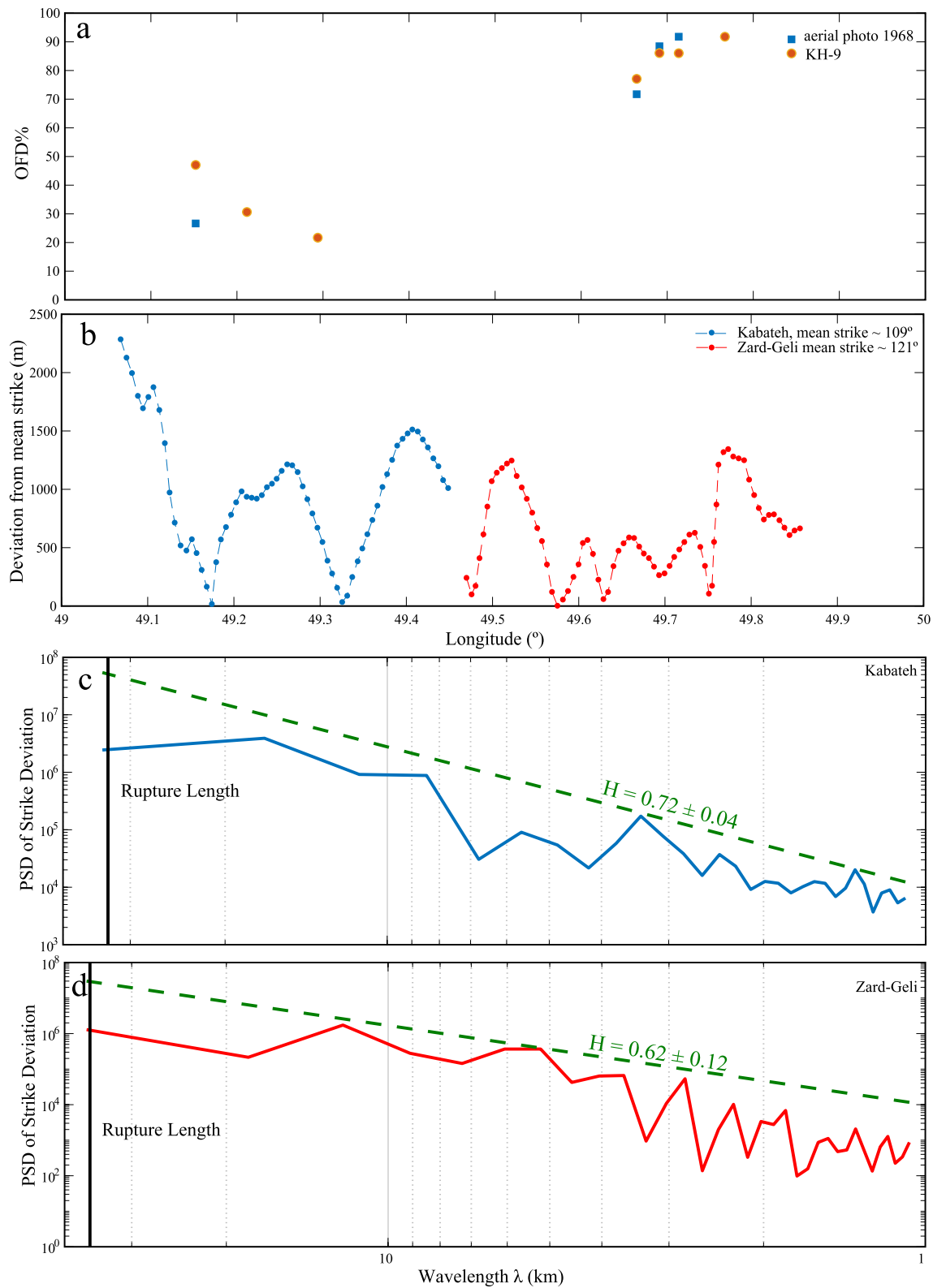
Figure 15. (a) Off-fault displacement (OFD) percentage for estimated from the difference of field and correlation offsets. (b) Deviation of the rupture strike from the mean for both Kabateh (blue) and Zard Geli (red), west and east of the Sefid Rud river, respectively. (c) and (d) Power Spectral Density (PSD) of the strike deviation and Hurst exponent coefficient (green dash line) for Kabateh (blue) and Zard Geli (red), respectively.

(Dolan & Haravitch, 2014). The Rudbar earthquake ruptured a structurally immature fault, given the low geological offsets (∼3 km) documented for this structure (Berberian & Walker, 2010; Hessami et al., 2003). Therefore, one may expect either enhanced SSD, or some significant proportion of OFD in this event, which is consistent with our estimates in Figure 15a.

Nevertheless, an important question concerns how reliable are the Rudbar field measurements, and do they warrant an analysis of OFD for the Rudbar earthquake? Compared with other large strike-slip earthquakes (e.g., Barnhart et al., 2020; Milliner et al., 2015; Zinke et al., 2019), we have very few points for comparison, thus limiting the statistical robustness of our analysis. Furthermore, the field measurements may not reflect the true degree of surface slip localization, and so any comparison will not reflect the real degree of OFD. Field mapping following the earthquake was highly challenging, given the destructive effects of the earthquake, problems in accessing the rupture in the high mountains, dense vegetation along the Zard Geli segment, a lack of well-expressed piercing points, and limited resources available for comprehensive rupture mapping in the aftermath of the earthquake (Manuel Berberian, pers. comm., 2020). For example, if slip became distributed across several parallel fault strands of equal displacement magnitude, and only one was mapped in the field because of access constraints, the localized slip that was not mapped will be attributed to OFD. It is also worth noting that this example also raises the issue of what is meant by OFD, and whether it represents purely inelastic distributed deformation, or includes localized slip that may be distributed across multiple secondary fault strands. A comparison is nevertheless useful here given the general lack of historical earthquake examples for which we have OFD measurements for; it is only by expanding our observations through the addition of new case studies that we can arrive at statistically robust conclusions over what factors control off-fault deformation or the localization of fault slip. In addition, it is not possible for us to quantitatively assess how good the field mapping was after the Rudbar earthquake, and so determine if our comparisons are valid or not. The Rudbar earthquake also represents a rare example of a structurally immature fault, which is confined entirely to the mountains; thus, the influence of topography will be more important than for case studies in more moderate terrain. Finally, the rupture cuts across both dry arid landscapes with limited vegetation (e.g., Kabateh), as well as dense vegetated areas (e.g., Zard Geli), and thus offers the potential for addressing how vegetation and soil development may impact surface slip localization.

The high degree of OFD estimates we report for this earthquake likely represent an upper bound, given the extreme difference with the seismic moment release. They are nevertheless broadly consistent with other examples from structurally immature faults, such as the 1992 Landers earthquake: 46% OFD (Milliner et al., 2015), and the 2018 Hualien earthquake: 60% OFD (Kuo et al., 2019).

5.4. Link Between OFD and Structural Complexity

The structural complexity (e.g., degree of segmentation, fault roughness) of several earthquake surface ruptures has been shown to correlate with OFD (Milliner et al., 2015, 2016; Zinke et al., 2014); less complex parts of the fault typically display lower OFD, while more complex sections show more localized slip. Our OFD estimates display a strong variation between Kabateh and Zard Geli segments (20%–50% vs. 70%–90%); therefore, we explore whether this variation may reflect differences in the structural complexity between these two fault segments.

The geometries of natural faults are known to be rough, possessing fractal scaling properties (e.g., Renard et al, 2006; Sagy et al., 2007; Sagy & Brodsky, 2009; Candela et al., 2009, 2012; Brodsky et al., 2011). The Hurst exponent (H) provides a measure of the self-similarity for rough fault surfaces. The slope of the power spectral density (PSD) (β) of slip, which is computed between the minimum wavelength and the fault segment length is related to the Hurst exponent by $H = (\beta-1)/2$ (Bruhat et al., 2020). $H = 1$ indicates a purely self-similar scaling, with RMS deviations from planarity being proportional to the fault length; self-similar fractals thus have a statistically similar appearance regardless of the observation scale (Bruhat et al., 2020). However, self-affine fractals ($H < 1$) appear smoother at larger scales; as faults become increasingly self-affine, they become rougher. Natural faults have been shown to possess self-affine scaling properties, with $H \approx 0.6$ (Renard et al., 2006; Candela et al. 2009, 2012).

We compute the H exponent for the Kabateh and Zard Geli fault segments based on the RMS deviation of the mapped rupture from planarity (Figures 15b–15d). Because scaling exponents estimated from the slope of the PSD can be biased (Di Matteo, 2007), we use the generalized Hurst exponent method (e.g., Aste, 2021; Di Matteo, 2007), which uses the qth-order moments of the distribution of the increments to quantify the scaling properties (the qth-order moments are much less sensitive to outliers than the minima and maxima). The generalized Hurst exponent is thus a highly robust, unbiased, and computationally efficient estimator, which describes well the scaling properties, even in the frequency domain. Both faults display self-affine scaling properties, although Kabateh ($H = 0.72$) appears less rough than Zard Geli ($H = 0.62$). Increased fault roughness may be expected to scale with OFD (e.g., Milliner et al., 2015, 2016), as more energy is lost, as inelastic deformation, to the volume surrounding the fault core as the rupture propagates through geometric complexities. Therefore, the larger values of OFD obtained along the Zard Geli segment are consistent with this hypothesis.

5.5. Fault Zone Width

In addition to estimating the absolute displacement across a fault, the distance between the minimum and maximum displacements from fault-perpendicular profiles can provide constraints on the FZW (FZW; e.g., Barnhart et al., 2020; Milliner et al., 2015; Zinke et al., 2019), which in turn may also reflect OFD; highly discrete slip will result in a sharp step across the displacement profile, while distributed slip over a wide fault zone will result in a smoothed discontinuity. The relationship between FZW, estimated from SPOT data, with rupture geometry and topography is not clear (Figures 11d–11f). FZW are also remarkably wide (600–1000 m), given the <100 m width of damage zones documented in other earthquakes (Barnhart et al., 2020; Milliner et al., 2016; Zinke et al., 2019), and from structural measurements (Mitchell & Faulkner 2009; Ostermeijer et al., 2020). Where the fault crosses Sefid Rud, the FZW is relatively large (>1 km), and possibly reflects an enhanced distribution of slip across mechanically weak sediments within the river valley.

Estimates of FZW from higher resolution aerial photos are shown in Figure 12c (and 16a for the Zard Geli segment), alongside estimates made from KH-9 and SPOT data; FZW decreases substantially with increasing image resolution. This raises doubts about the ability of medium resolution optical satellite datasets (e.g., SPOT1-4, Landsat-8, or Sentinel-2) to reliably capture information about FZW. Because correlation windows require enough long-wavelength information to obtain a reliable displacement, which in turn requires larger windows, any discontinuity in the displacement field becomes smoothed by the correlation process (by ~50% of the correlation window size for COSI-Corr, due to the use of a windowing function when computing the FFT, see Milliner et al., 2015). Therefore, displacement maps are often computed with a sparse ground sampling, e.g., half the window dimension. In COSI-Corr, the minimum recommended correlation window size to avoid substantial sub-pixel bias is 32 pixels. Therefore displacements should be computed every 16 pixels to obtain independent measurements; denser sampling will amount to oversampling, and thus not provide any significant increase in the level of spatial detail (though can be useful for reducing the impact of noise). In our SPOT correlations, we compute the displacement every eight pixels, giving a displacement map with a pixel resolution of 80 m. Fault zones of ~200 m width (damage zones of 100 m) would therefore only represent ~20 pixels in a SPOT (10 m) image, and only 2.5 pixels in the resulting displacement map. Given the relatively low signal-to-noise ratio in SPOT correlations, FZW estimates will also be strongly biased by noise, thus rendering it highly challenging to measure FZW from SPOT data. Finer sampling of the displacement map can be achieved (e.g., with correlators such as MicMac), however the displacements will still be impacted by smoothing, which adds uncertainty to the FZW estimate. Smoothing across the fault results broadens the inferred width of the fault zone (Figure 17a). As smoothing increases, the roll-over of the fault offset makes measurement of the FZW more uncertain (especially in the presence of noise).

As we know the smoothing bias to be expected, from the correlation window size used plus any subsequent smoothing applied, we can then correct the FZW estimated with lower resolution data. Figure 16a shows the FZW estimates for SPOT, KH9, and aerial photos for the Zard Geli segment. The average widths in the overlapping area are given as a function of the input image resolution in Figure 16b; the blue line indicates the smoothing bias introduced by the correlation process. The linear relationship between different resolutions provides an empirical way to correct FZW estimated from SPOT data. Nevertheless, the average
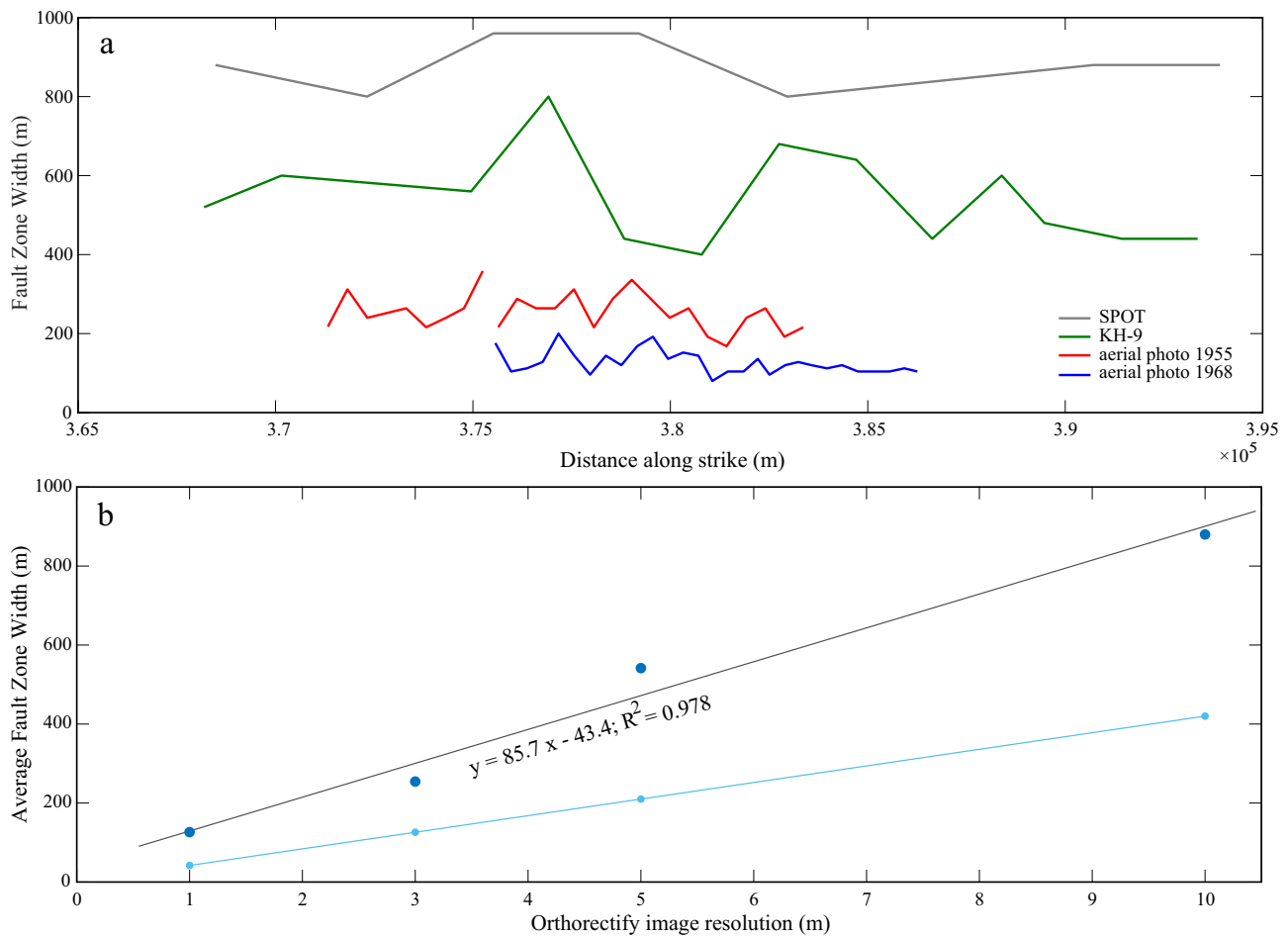
Figure 16. (a) Fault zone width (FZW) for the part of Zard Geli, where all data sets are overlapping: SPOT (dark gray line), KH9 (green), 1955–2001/3 aerial (red), and 1968–2001/3 aerial (blue). (b) Average FZW for each data set in (a), as a function of the input orthoimage resolution. Gray line presents the first-order of fitting line. Blue curve shows the minimum FZW bias which comes from smoothing associated with the correlator and additional 3 × 3 median smoothing.

displacement increases with pixel size more than expected based purely on the correlation smoothing bias. The reason for this is likely due to the self-affine properties of the fault rupture. To increase the signal-to-noise ratio of the SPOT data, we stack fault-perpendicular profiles within a box oriented (on average) perpendicular to the fault. However, any geometric variability of the fault within this box will result in artificially smoothing the FZW (Figures 17a and 17b). Because the amplitude of geometric variability increases at longer wavelengths, the larger widths used in stacked SPOT displacement profiles will result in greater geometric smoothing bias compared with smaller stacked windows used with aerial photo correlations. Using the mapped rupture trace, we estimate the contribution of geometric smoothing bias on the SPOT FZW estimates (Figure 17c) and find it to contribute significantly. Therefore, the increase in FZW with lower resolution data will vary for different earthquakes based on the scaling properties of the fault rupture (geometric) roughness. If this can be characterized based on the mapped fault trace, this may offer a potential way to estimate the geometric smoothing bias, and thus infer reliable FZW estimates from lower resolution optical data.

We also note that FZW estimates made from aerial photos may also be subject to the same geometry and correlation smoothing bias, and therefore even higher resolution data will be required to reliably capture the true widths. However, the FZW estimates from 1 m aerial photos for Zard Geli (Figure 16) are generally <50 m (when accounting for correlator and geometric smoothing), which is similar to those made for the 1992 Landers earthquake (Milliner et al., 2015) and 2016 Kaikoura earthquake (Zinke et al., 2019), as well as field-based structural observations of damage zone widths (Mitchell & Faulkner 2009; Ostermeijer
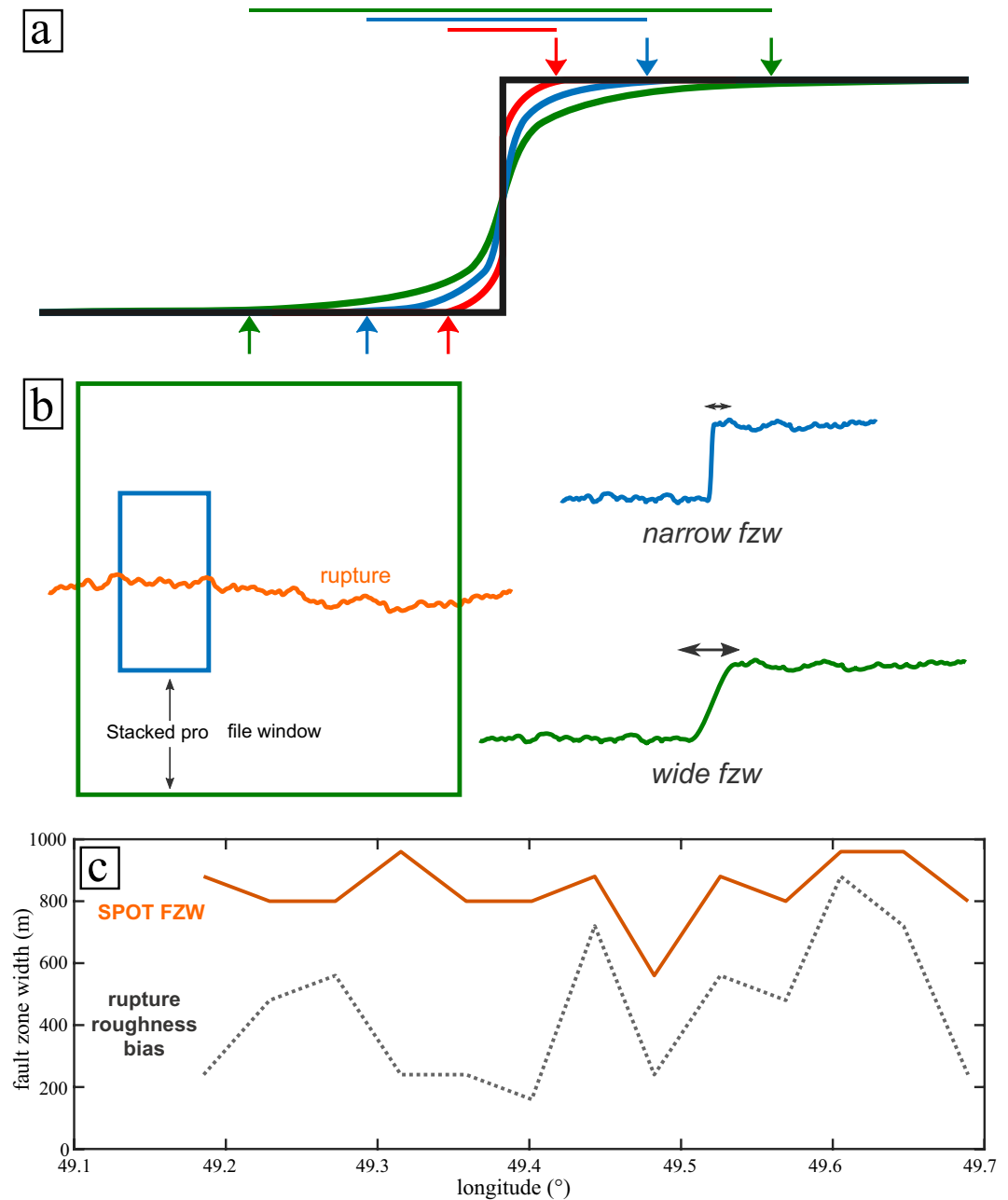
Figure 17. (a) Smoothing associated with the correlation process will artificially smooth the discrete fault offset estimate. As the correlation window becomes wider, the smoothing becomes increasingly strong. Estimation of the fault zone width (FZW) becomes increasingly more challenging, especially in the presence of noise. (b) Small (blue) and wide (green) stacked profiles will capture different scales of geometric complexity, which in turn will artificially smooth (widen) the FZW estimate. (c) FZW estimates along-strike of the Rudbar fault, from SPOT data (orange). Dashed gray line shows the artificial contribution to FZW which comes purely form geometric complexity within the stacked profile box.

et al., 2020). This is likely because (1) the aerial photo correlations sample the damage zones with sufficient density to accurately capture real off-fault deformation with minimal bias due to smoothing, and (2) at finer scales the amplitude of variability is smaller. The FZW for the Kabateh and Zard Geli segments appears relatively similar (over wavelengths of several km); both segments generally rupture through bedrock, which may explain the relatively narrow damage zones.
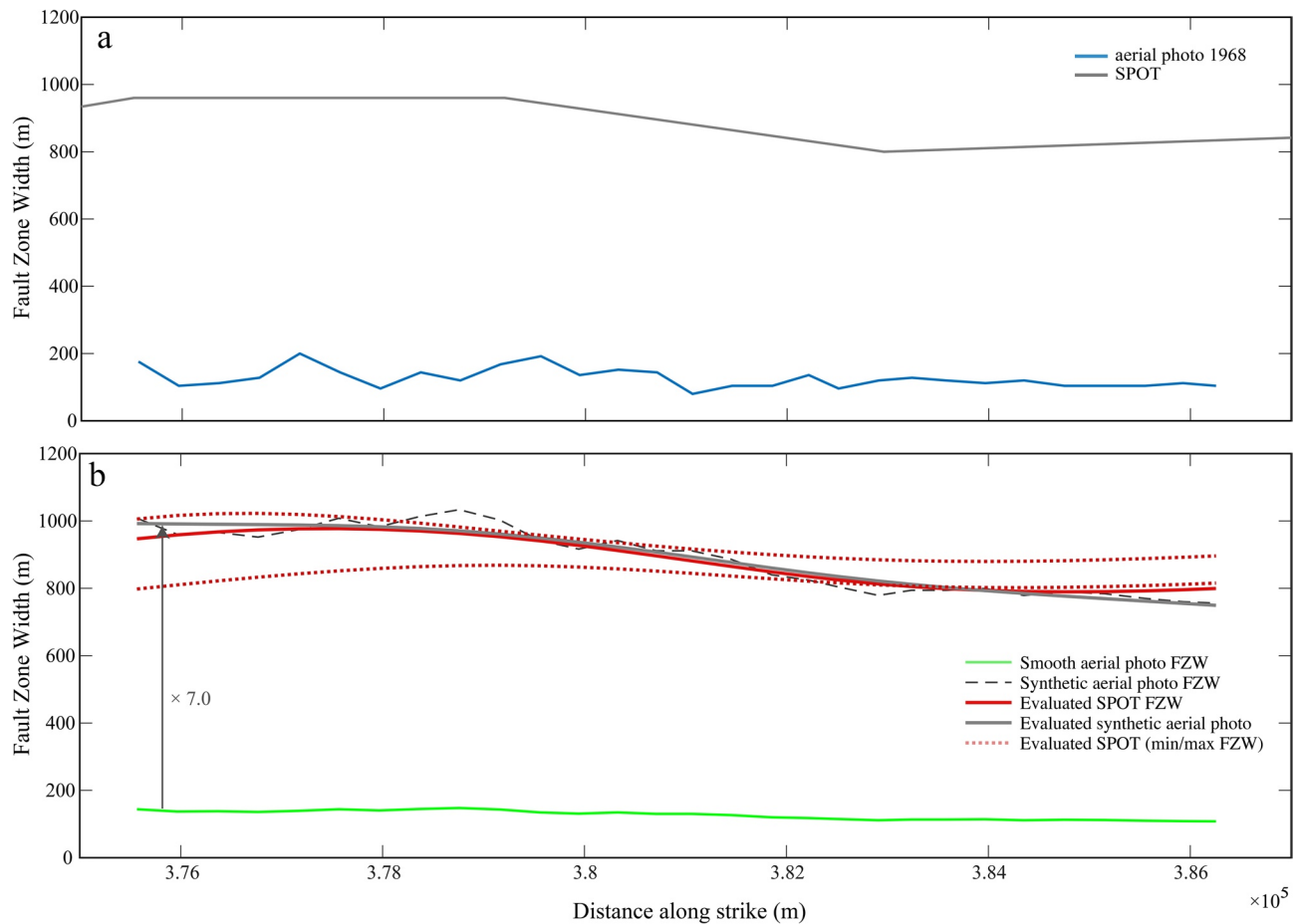
Figure 18. (a) Fault zone width in the part of Zard Geli, where all data sets are overlapping the same area. SPOT fault zone width (FWZ) (gray line), and 1968–2001/3 aerial FZW (blue line). (b) Smoothed aerial photo FZW (light green), amplified by nine to create a synthetic SPOT FZW (gray line). Dashed gray line shows the amplified, but unsmoothed FZW. SPOT FZW interpolated with a smoothing spline (red); min and max estimates shown as dashed red lines. The similarity between the solid red and gray curves highlights the long-wavelength FZW variability present within the SPOT FZW measurements. The two-sample Kolmogorov-Smirove test shows the two distributions are the statistically similar (at the 5% significance level).

While the FZW estimates from SPOT data may be corrected in an absolute sense, does the along-strike variability in FZW also reflect real variation recorded in higher resolution data? To address this, we smooth the aerial photo FZW estimates for a section of the Zard Geli fault (Figure 18a) segment to an equivalent spatial wavelength reflected by the SPOT data (Figure 18b), before adjusting them to account for the amplitude bias seen with SPOT FZW estimates (Figures 16a and 18a). We find these "synthetic" FZW estimates agree well with the raw SPOT estimates; a two-sample Kolmogorov-Smirnov test confirms that the two curves follow the same distribution (at the 5% significance level). This observation suggests that although the lower resolution of SPOT data impacts our ability to resolve useful information about FZW, the spatial variability captured in lower resolution SPOT data may nevertheless preserve real information at longer wavelengths. These observations are important for how we interpret details of the near-field strain around fault ruptures using medium resolution (5–15 m) satellite data, which is more widely available than high resolution imagery.

6. Conclusion

We develop a novel workflow to generate pre- and post-earthquake DEMs and orthorectified images using stereo aerial photos. We then mosaiced all ortho-images and correlate pre- and post-earthquake orthomosaics to obtain the surface displacement pattern for the 1990 Rudbar earthquake, which facilitates the measurement of the coseismic slip distribution and FZW at the surface. We complement the aerial photos with

satellite imagery, of lower resolution, which covers a broader region around the fault. In this case, we use SPOT and ortho KH9 images with resolutions of 10 and 5 m, respectively. The left-lateral slip distribution indicates a dramatic increase in slip ∼30 km east of the epicenter on the Zard Geli segment (maximum offset ∼5.5 m), with minor fault-normal and vertical components related to local variations in the fault strike and dip. The average left-lateral slip for the observed rupture is ∼2.2 m with a FZW of ∼100 m (for the parts of the faults covered by aerial photos). Slip appears to be continuous across the Sefid Rud river valley, although no clear sign of localized surface rupture is visible in the correlation data, suggesting either a decrease in slip near the surface, or highly distributed slip over a broad zone. We document a new 10–15 km rupture on the Hajideh Fault (also either blind or highly distributed), which may represent a continuation of the Kabateh segment east of Sefid Rud. Significant off-fault deformation may be associated with the Rudbar earthquake, which is consistent with the apparent low structural maturity of the Rudbar fault. Our approach can be easily applied to other historical events that occurred after mid twentieth century when aerial photos are available, to better document past surface ruptures, as well as future events, especially when very high resolution drone imagery is available.

Data Availability Statement

KH-9 satellite imagery and 1955 USGS aerial photos were obtained from the Earth Explorer website (http://earthexplorer.usgs.gov/). SPOT images were acquired through the DINAMIS program. Sentinel-2 imagery was obtained from ESA (https://scihub.copernicus.eu/). We processed all optical data sets using the open-source Ames Stereo Pipeline (ASP) software package, developed by NASA (Beyer et al., 2018).

References

Alavi, M. (1996). Tectonostratigraphic synthesis and structural style of the Alborz mountain system in northern Iran. *Journal of Geodynamics*, *21*(1), 1–33. https://doi.org/10.1016/0264-3707(95)00009-7

Allen, M. B., Ghassemi, M. R., Shahrabi, M., & Qorashi, M. (2003). Accommodation of late Cenozoic oblique shortening in the Alborz range, northern Iran. *Journal of Structural Geology*, *25*(5), 659–672. https://doi.org/10.1016/s0191-8141(02)00064-0

Ambraseys, N. N., & Melville, C. P. (2005). *A history of Persian earthquakes*. Cambridge university press.

Aste, T. (2021). *Generalized Hurst exponent*. In MATLAB Central File Exchange. Retrieved from https://www.mathworks.com/matlabcentral/fileexchange/30076-generalized-hurst-exponent

Avouac, J. P., Ayoub, F., Leprince, S., Konca, O., & Helmberger, D. V. (2006). The 2005, Mw 7.6 Kashmir earthquake: Sub-pixel correlation of ASTER images and seismic waveforms analysis. *Earth and Planetary Science Letters*, *249*(3–4), 514–528. https://doi.org/10.1016/j.epsl.2006.06.025

Avouac, J. P., & Leprince, S. (2015). Geodetic imaging using optical systems. *Geodesy* (pp. 387–424). https://doi.org/10.1016/b978-0-444-53802-4.00067-1

Ayoub, F., Leprince, S., & Avouac, J. P. (2009). Co-registration and correlation of aerial photographs for ground deformation measurements. *ISPRS Journal of Photogrammetry and Remote Sensing*, *64*(6), 551–560. https://doi.org/10.1016/j.isprsjprs.2009.03.005

Aziz Zanjani, A., Ghods, A., Sobouti, F., Bergman, E., Mortezanejad, G., Priestley, K., et al. (2013). Seismicity in the western coast of the South Caspian Basin and the Talesh Mountains. *Geophysical Journal International*, *195*(2), 799–814. https://doi.org/10.1093/gji/ggt299

Barnhart, W. D., Gold, R. D., & Hollingsworth, J. (2020). Localized fault-zone dilatancy and surface inelasticity of the 2019 Ridgecrest earthquakes. *Nature Geoscience*, *13*(10), 699–704. https://doi.org/10.1038/s41561-020-0628-8

Berberian, M. (1983). The southern Caspian: A compressional depression floored by a trapped, modified oceanic crust. *Canadian Journal of Earth Sciences*, *20*(2), 163–183. https://doi.org/10.1139/e83-015

Berberian, M., & Qorashi, M. (1984). Recent tectonics, seismotectonics and earthquake-fault hazard study of the Zanjan Lead-Zinc Melting Plant. *Report - Geological Survey of Iran*.

Berberian, M., Qorashi, M., Arzhangravesh, B., & Mohajer-Ashjai, A. (1983). Recent tectonics, Seismotectonics, and earthquake-fault hazard study of the greater Qazvin area. *Geological Survey of Iran*, *57*, 84.

Berberian, M., Qorashi, M., Jackson, J. A., Priestley, K., & Wallace, T. (1992). The Rudbar-Tarom earthquake of 20 June 1990 in NW Persia: Preliminary field and seismological observations, and its tectonic significance. *Bulletin of the Seismological Society of America*, *82*(4), 1726–1755.

Berberian, M., & Walker, R. (2010). The Rudbār Mw 7.3 earthquake of 1990 June 20; seismotectonics, coseismic and geomorphic displacements, and historic earthquakes of the western 'High-Alborz', Iran. *Geophysical Journal International*, *182*(3), 1577–1602. https://doi.org/10.1111/j.1365-246x.2010.04705.x

Beyer, R. A., Alexandrov, O., & McMichael, S. (2018). The Ames Stereo Pipeline: NASA's open source software for deriving and processing terrain data. *Earth and Space Science*, *5*(9), 537–548. https://doi.org/10.1029/2018ea000409

Brodsky, E. E., Gilchrist, J. J., Sagy, A., & Collettini, C. (2011). Faults smooth gradually as a function of slip. *Earth and Planetary Science Letters*, *302*(1–2), 185–193. https://doi.org/10.1016/j.epsl.2010.12.010

Broxton, M. J., & Edwards, L. J. (2008). The Ames Stereo Pipeline: Automated 3D surface reconstruction from orbital imagery. In Lunar and Planetary Science Conference (1391, p. 2419).

Bruhat, L., Klinger, Y., Vallage, A., & Dunham, E. M. (2020). Influence of fault roughness on surface displacement: From numerical simulations to coseismic slip distributions. *Geophysical Journal International*, *220*(3), 1857–1877. https://doi.org/10.1093/gji/ggz545

Campos, J., Madariaga, R., Nábělek, J., Bukchin, B. G., & Deschamps, A. (1994). Faulting process of the 1990 June 20 Iran earthquake from broadband records. *Geophysical Journal International*, *118*(1), 31–46. https://doi.org/10.1111/j.1365-246x.1994.tb04673.x

Candela, T., Renard, F., Bouchon, M., Brouste, A., Marsan, D., Schmittbuhl, J., & Voisin, C. (2009). Characterization of fault roughness at various scales: Implications of three-dimensional high resolution topography measurements. In Mechanics, structure and evolution of fault zones. 166, 1817–1851. https://doi.org/10.1007/978-3-0346-0138-2_13

Candela, T., Renard, F., Klinger, Y., Mair, K., Schmittbuhl, J., & Brodsky, E. E. (2012). Roughness of fault surfaces over nine decades of length scales. *Journal of Geophysical Research*, *117*(B8). https://doi.org/10.1029/2011jb009041

Chester, F. M., & Chester, J. S. (1998). Ultracataclasite structure and friction processes of the San Andreas Fault. *Tectonophysics*, *295*, 199–221. https://doi.org/10.1016/s0040-1951(98)00121-8

Choy, G. L., & Zedník, J. (1997). The rupture process of the Manjil, Iran earthquake of 20 June 1990 and Implications for intraplate strike-slip earthquakes. *Studia Geophysica et Geodaetica*, *41*(1), 45–63. https://doi.org/10.1023/a:1023336723587

Das, S., & Henry, C. (2003). Spatial relation between main earthquake slip and its aftershock distribution. *Reviews of Geophysics*, *41*(3). 1013. https://doi.org/10.1029/2002rg000119

Di Matteo, T. (2007). Multi-scaling in finance. *Quantitative Finance*, *7*(1), 21–36. https://doi.org/10.1080/14697680600969727

Djamour, Y., Vernant, P., Bayer, R., Nankali, H. R., Ritz, J. F., Hinderer, J., et al. (2010). GPS and gravity constraints on continental deformation in the Alborz mountain range, Iran. *Geophysical Journal International*, *183*(3), 1287–1301. https://doi.org/10.1111/j.1365-246x.2010.04811.x

Dolan, J. F., & Haravitch, B. D. (2014). How well do surface slip measurements track slip at depth in large strike-slip earthquakes? The importance of fault structural maturity in controlling on-fault slip versus off-fault surface deformation. *Earth and Planetary Science Letters*, *388*, 38–47. https://doi.org/10.1016/j.epsl.2013.11.043

Engdahl, E. R., Jackson, J. A., Myers, S. C., Bergman, E. A., & Priestley, K. (2006). Relocation and assessment of seismicity in the Iran region. *Geophysical Journal International*, *167*(2), 761–778. https://doi.org/10.1111/j.1365-246x.2006.03127.x

Fialko, Y., Sandwell, D., Simons, M., & Rosen, P. (2005). Three-dimensional deformation caused by the Bam, Iran, earthquake and the origin of shallow slip deficit. *Nature*, *435*(7040), 295–299. https://doi.org/10.1038/nature03425

Gao, L., & Wallace, T. C. (1995). The 1990 Rudbar-Tarom Iranian earthquake sequence: Evidence for slip partitioning. *Journal of Geophysical Research*, *100*(B8), 15317–15332. https://doi.org/10.1029/95jb00320

Gao, L., Wallace, T. C., & Jackson, J. A. (1991). Aftershocks of the June 1990 Rudbar-Tarom earthquake: Evidence for slip partitioning. *Eos Transactions American Geophysical Union*, *72*, 44.

Ghods, A., Rezapour, M., Bergman, E., Mortezanejad, G., & Talebian, M. (2012). Relocation of the 2006 Mw 6.1 Silakhour, Iran, earthquake sequence: details of fault segmentation on the main recent fault. *Bulletin of the Seismological Society of America*, *102*(1), 398–416. https://doi.org/10.1785/0120110009

Ghods, A., Shabanian, E., Bergman, E., Faridi, M., Donner, S., Mortezanejad, G., & Aziz-Zanjani, A. (2015). The Varzaghan–Ahar, Iran, Earthquake Doublet (M$_w$ 6.4, 6.2): Implications for the geodynamics of northwest Iran. *Geophysical Journal International*, *203*(1), 522–540. https://doi.org/10.1093/gji/ggv306

Hessami, K., Jamali, F., & Tabassi, H. (2003). Major active faults of Iran (map), scale 1: 2, 5000, 000, Ministry of Science. *Research and Technology, International Institute of Earthquake Engineering and Seismology*.

Jackson, J., Priestley, K., Allen, M., & Berberian, M. (2002). Active tectonics of the south Caspian basin. *Geophysical Journal International*, *148*(2), 214–245. https://doi.org/10.1046/j.1365-246x.2002.01005.x

Khorrami, F., Vernant, P., Masson, F., Nilfouroushan, F., Mousavi, Z., Nankali, H., et al. (2019). An up-to-date crustal deformation map of Iran using integrated campaign-mode and permanent GPS velocities. *Geophysical Journal International*, *217*(2), 832–843. https://doi.org/10.1093/gji/ggz045

Kuo, Y. T., Wang, Y., Hollingsworth, J., Huang, S. Y., Chuang, R. Y., Lu, C. H., et al. (2019). Shallow fault rupture of the Milun fault in the 2018 Mw 6.4 Hualien earthquake: A high-resolution approach from optical correlation of Pléiades satellite imagery. *Seismological Research Letters*, *90*(1), 97–107. https://doi.org/10.1785/0220180227

Lacroix, P., Araujo, G., Hollingsworth, J., & Taipe, E. (2019). Self-entrainment motion of a slow-moving landslide inferred from landsat-8 time series. *Journal of Geophysical Research: Earth Surface*, *124*(5), 1201–1216. https://doi.org/10.1029/2018jf004920

Leprince, S., Barbot, S., Ayoub, F., & Avouac, J. P. (2007). Automatic and precise orthorectification, coregistration, and subpixel correlation of satellite images, application to ground deformation measurements. *IEEE Transactions on Geoscience and Remote Sensing*, *45*(6), 1529–1558. https://doi.org/10.1109/tgrs.2006.888937

Madanipour, S., Ehlers, T. A., Yassaghi, A., & Enkelmann, E. (2017). Accelerated middle Miocene exhumation of the Talesh Mountains constrained by U-Th/He thermochronometry: Evidence for the Arabia-Eurasia collision in the NW Iranian Plateau. *Tectonics*, *36*(8), 1538–1561. https://doi.org/10.1002/2016tc004291

Marchandon, M., Vergnolle, M., Cavalié, O., Sudhaus, H., & Hollingsworth, J. (2018). Earthquake sequence in the NE Lut, Iran: Observations from multiple space geodetic techniques. *Geophysical Journal International*, *215*(3), 1604–1621. https://doi.org/10.1093/gji/ggy364

Milliner, C. W. D., Dolan, J. F., Hollingsworth, J., Leprince, S., & Ayoub, F. (2016). Comparison of coseismic near-field and off-fault surface deformation patterns of the 1992 Mw 7.3 Landers and 1999 Mw 7.1 Hector Mine earthquakes: Implications for controls on the distribution of surface strain. *Geophysical Research Letters*, *43*(19), 10–115. https://doi.org/10.1002/2016gl069841

Milliner, C. W. D., Dolan, J. F., Hollingsworth, J., Leprince, S., Ayoub, F., & Sammis, C. G. (2015). Quantifying near-field and off-fault deformation patterns of the 1992 Mw 7.3 Landers earthquake. *Geochemistry, Geophysics, Geosystems*, *16*(5), 1577–1598. https://doi.org/10.1002/2014gc005693

Mitchell, T. M., & Faulkner, D. R. (2009). The nature and origin of off-fault damage surrounding strike-slip fault zones with a wide range of displacements: A field study from the Atacama fault system, northern Chile. *Journal of Structural Geology*, *31*(8), 802–816. https://doi.org/10.1016/j.jsg.2009.05.002

Oskin, M. E., Arrowsmith, J. R., Corona, A. H., Elliott, A. J., Fletcher, J. M., Fielding, E. J, et al. (2012). Near-field deformation from the El Mayor–Cucapah earthquake revealed by differential LIDAR. *Science*, *335*(6069), 702–705. https://doi.org/10.1126/science.1213778

Ostermeijer, G. A., Mitchell, T. M., Aben, F. M., Dorsey, M. T., Browning, J., Rockwell, T. K., & Ostermeijer, F. (2020). Damage zone heterogeneity on seismogenic faults in crystalline rock; a field study of the Borrego Fault, Baja California. *Journal of Structural Geology*, *137*, 104016. https://doi.org/10.1016/j.jsg.2020.104016

Pomerleau, F., Colas, F., Siegwart, R., & Magnenat, S. (2013). Comparing ICP variants on real-world data sets. *Autonomous Robots*, *34*(3), 133–148. https://doi.org/10.1007/s10514-013-9327-2

Rahmani, M., Motaghi, K., Ghods, A., Sobouti, F., Talebian, M., Ai, Y., & Chen, L. (2019). Deep velocity image of the north Zagros collision zone (Iran) from regional and teleseismic tomography. *Geophysical Journal International*, *219*(3), 1729–1740. https://doi.org/10.1093/gji/ggz393

Renard, F., Voisin, C., Marsan, D., & Schmittbuhl, J. (2006). High resolution 3D laser scanner measurements of a strike-slip fault quantify its morphological anisotropy at all scales. *Geophysical Research Letters*, *33*(4), 33–36. https://doi.org/10.1029/2005GL025038

Rezaeian, M., Carter, A., Hovius, N., & Allen, M. B. (2012). Cenozoic exhumation history of the Alborz Mountains, Iran: New constraints from low-temperature chronometry. *Tectonics*, *31*(2). https://doi.org/10.1029/2011tc002974

Rezaeian, M., Kuijper, C. B., van der Boon, A., Pastor-Galán, D., Cotton, L. J., Langereis, C. G., & Krijgsman, W. (2020). Post-Eocene coupled oroclines in the Talesh (NW Iran): Paleomagnetic constraints. *Tectonophysics*, *786*, 228459. https://doi.org/10.1016/j.tecto.2020.228459

Rockwell, T. K., Lindvall, S., Dawson, T., Langridge, R., Lettis, W., & Klinger, Y. (2002). Lateral offsets on surveyed cultural features resulting from the 1999 Izmit and Duzce earthquakes, Turkey. *Bulletin of the Seismological Society of America*, *92*(1), 79–94. https://doi.org/10.1785/0120000809

Rosu, A. M., Pierrot-Deseilligny, M., Delorme, A., Binet, R., & Klinger, Y. (2015). Measurement of ground displacement from optical satellite image correlation using the free open-source software MicMac. *ISPRS Journal of Photogrammetry and Remote Sensing*, *100*, 48–59. https://doi.org/10.1016/j.isprsjprs.2014.03.002

Sagy, A., & Brodsky, E. E. (2009). Geometric and rheological asperities in an exposed fault zone. *Journal of Geophysical Research*, *114*(B2), B02301. https://doi.org/10.1029/2008jb005701

Sagy, A., Brodsky, E. E., & Axen, G. J. (2007). Evolution of fault-surface roughness with slip. *Geology*, *35*(3), 283–286. https://doi.org/10.1130/g23235a.1

Schwartz, D. P., Haeussler, P. J., Seitz, G. G., & Dawson, T. E. (2012). Why the 2002 Denali fault rupture propagated onto the Totschunda fault: Implications for fault branching and seismic hazards. *Journal of Geophysical Research*, *117*(B11), B11304. https://doi.org/10.1029/2011jb008918

Shean, D. E., Alexandrov, O., Moratto, Z. M., Smith, B. E., Joughin, I. R., Porter, C., & Morin, P. (2016). An automated, open-source pipeline for mass production of digital elevation models (DEMs) from very-high-resolution commercial stereo satellite imagery. *ISPRS Journal of Photogrammetry and Remote Sensing*, *116*, 101–117. https://doi.org/10.1016/j.isprsjprs.2016.03.012

Socquet, A., Hollingsworth, J., Pathier, E., & Bouchon, M. (2019). Evidence of supershear during the 2018 magnitude 7.5 Palu earthquake from space geodesy. *Nature Geoscience*, *12*(3), 192–199. https://doi.org/10.1038/s41561-018-0296-0

Stöcklin, J. (1974). Possible ancient continental margins in Iran. In The geology of continental margins (pp. 873–887). Springer. https://doi.org/10.1007/978-3-662-01141-6_64

Tatar, M., & Hatzfeld, D. (2009). Microseismic evidence of slip partitioning for the Rudbar-Tarom earthquake (Ms 7.7) of 1990 June 20 in NW Iran. *Geophysical Journal International*, *176*(2), 529–541. https://doi.org/10.1111/j.1365-246x.2008.03976.x

Teknik, V., Ghods, A., Thybo, H., & Artemieva, I. M. (2019). Crustal density structure of the northwestern Iranian Plateau. *Canadian Journal of Earth Sciences*, *56*(12), 1347–1365. https://doi.org/10.1139/cjes-2018-0232

Thio, H. K., Satake, K., Kikuchi, M., & Kanamori, H. (1990). On the Sudan, Iran, and Philippines earthquakes of 1990. *Eos Transactions American Geophysical Union*, *71*, 1438.

Tsai, R. (1987). A versatile camera calibration technique for high-accuracy 3D machine vision metrology using off-the-shelf TV cameras and lenses. *IEEE Journal of Robotics and Automation*, *3*(4), 323–344. https://doi.org/10.1109/jra.1987.1087109

Vallage, A., Klinger, Y., Lacassin, R., Delorme, A., & Pierrot-Deseilligny, M. (2016). Geological structures control on earthquake ruptures: The Mw7. 7, 2013, Balochistan earthquake, Pakistan. *Geophysical Research Letters*, *43*(19), 10–155. https://doi.org/10.1002/2016gl070418

Vernant, P., Nilforoushan, F., Chery, J., Bayer, R., Djamour, Y., Masson, F., et al. (2004). Deciphering oblique shortening of central Alborz in Iran using geodetic data. *Earth and Planetary Science Letters*, *223*(1–2), 177–185. https://doi.org/10.1016/j.epsl.2004.04.017

Vernant, P., Nilforoushan, F., Hatzfeld, D., Abbassi, M. R., Vigny, C., Masson, F., et al. (2004). Present-day crustal deformation and plate kinematics in the Middle East constrained by GPS measurements in Iran and northern Oman. *Geophysical Journal International*, *157*(1), 381–398. https://doi.org/10.1111/j.1365-246x.2004.02222.x

Xu, X., Tong, X., Sandwell, D. T., Milliner, C. W. D., Dolan, J. F., Hollingsworth, J., et al. (2016). Refining the shallow slip deficit. *Geophysical Journal International*, *204*(3), 1867–1886. https://doi.org/10.1093/gji/ggv563

Zhou, Y., Walker, R. T., Hollingsworth, J., Talebian, M., Song, X., & Parsons, B. (2016). Coseismic and postseismic displacements from the 1978 Mw 7.3 Tabas-e-Golshan earthquake in eastern Iran. *Earth and Planetary Science Letters*, *452*, 185–196. https://doi.org/10.1016/j.epsl.2016.07.038

Zinke, R., Hollingsworth, J., & Dolan, J. F. (2014). Surface slip and off-fault deformation patterns in the 2013 MW 7.7 Balochistan, Pakistan earthquake: Implications for controls on the distribution of near-surface coseismic slip. *Geochemistry, Geophysics, Geosystems*, *15*(12), 5034–5050. https://doi.org/10.1002/2014gc005538

Zinke, R., Hollingsworth, J., Dolan, J. F., & Van Dissen, R. (2019). Three-dimensional surface deformation in the 2016 MW 7.8 Kaikōura, New Zealand, earthquake from optical image correlation: Implications for strain localization and long-term evolution of the Pacific-Australian plate boundary. *Geochemistry, Geophysics, Geosystems*, *20*(3), 1609–1628. https://doi.org/10.1029/2018gc007951